Raman scattering of spin-$\frac{1}{2}$ mixed-dimensionality antiferromagnetic α-$Cu_2V_2O_7$

Hemant Singh Kunwar,[1] Isha,[1] Arvind Kumar Yogi,[1,*] Binoy Krishna De,[1] Vivek Dwij,[2] Mayanak Kumar Gupta,[3,4] R. Mittal,[3,4] R. Venkatesh,[1] R. J. Chaudhary,[1] Mahesh Vedpathak,[5] and V. G. Sathe[1,†]

[1]*UGC-DAE Consortium for Scientific Research, University Campus, Khandwa Road, Indore 452001, India*
[2]*Department of Condensed Matter Physics and Material Science, Tata Institute of Fundamental Research, Homi Bhabha Road, Colaba, Mumbai 400005,India*
[3]*Solid State Physics Division, Bhabha Atomic Research Centre, Trombey, Mumbai 400005, India*
[4]*Homi Bhabha National Institute, Mumbai 400094, India*
[5]*Department of Physics, Vidya Pratishthan's Arts, Science and Commerce, Baramati 413133, India*

(Received 15 August 2023; revised 9 November 2023; accepted 13 December 2023; published 21 February 2024)

We present a detailed investigation of the lattice vibrations and magnetic properties of the spin-$\frac{1}{2}$ α-$Cu_2V_2O_7$ system by means of x-ray diffraction (XRD), magnetic susceptibility, specific heat, x-ray absorption spectroscopy (XAS), x-ray photoelectron spectroscopy (XPS), and Raman scattering measurements along with a phonon structure calculations by density-functional theory (DFT). Thermodynamic measurements show a long-range ordered (LRO) state at Néel temperature $T_N \sim 33.4$ K. From the molar susceptibility curves analysis an effective magnetic moment of 1.83 μ_B and an antiferromagnetic intrachain exchange coupling of ~62.13 K (~5.35 meV) is deduced. Despite exchange coupling in 1D chains, the susceptibility, low-temperature heat-capacity, and Raman spectroscopic analysis confirms that the antiferromagnetic order emerges from the mixed dimensionality nature of the exchange couplings and interchain exchange coupling was found to be ~16.91 K. Temperature-dependent Raman spectra has been performed in the temperature range 3.5 K to 300 K and established the spin-lattice coupling below 50 K, which appears well above T_N and is attributed to short-range magnetic ordering (T_{SRO}). The spin-lattice coupling constant has been calculated for various modes. Further, the detailed study of lattice dynamics by first-principle calculations on α-$Cu_2V_2O_7$ is presented.

DOI: 10.1103/PhysRevB.109.054310

I. INTRODUCTION

The low-dimensional quantum magnets can show strong quantum fluctuations in the lattice and are therefore interesting because these quantum fluctuations significantly influence the magnetic ground states. The Heisenberg isotropic spin-$\frac{1}{2}$ chain with antiferromagnetic exchange-couplings between nearest neighbors (NNs) and next-nearest neighbors (NNNs) is the simplest frustrated quantum system, which reveals a collective behavior arising from the quantum fluctuations [1,2]. The one-dimensional (1D) zigzag chains system offers interplay between magnetic-lattice (geometrical) frustration, quantum fluctuations, and long-range magnetic ordering and is therefore one of the central research topics in both theoretical and experimental condensed matter physics [3–10]. Moreover, the 1D quantum magnets are crucial because these quantum materials provide a unique opportunity to investigate both ground and excited states of existing quantum models [7,11]. The competing 1D or quasi-1D interactions due to quantum and thermal fluctuations favor a continuous symmetry at zero or any finite temperature as explained in the Mermin and Wagner theorem [12]. In such systems the long-range magnetic order does not exist and the magnetic lattice may show a spin liquid phase [13]. However, the magnetic excitation of 1D chains system behaves differently for a half-integer and an integer spin state. For instance, a quantum antiferromagnet with spin-$\frac{1}{2}$ 1D system exhibit gapless excitations [5], whereas spin-1 systems exhibit gaped excitations, which provide a possibility of Haldane gap formation [6].

The family of pyrovanadates $M_2V_2O_7$ (M = Cu, Ni, Co, Mn) offers 1D chains and hence provide opportunities to study enhanced quantum fluctuations and its effects on the ground-state and magnetic properties. We chose α-$Cu_2V_2O_7$ as it offers competing 1D chains and quasi-2D helical-honeycomb magnetic structure [14–16]. α-$Cu_2V_2O_7$ is a quantum spin magnet, which offers to study mixed dimensionality as 1D and quasi-2D magnetic lattices and involved structural dynamics. The $Cu_2V_2O_7$ compound have two different forms of phases (i) low-temperature (LT) phase known as α with orthorhombic crystal structure and $Fdd2$ symmetry and (ii) high-temperature (HT) phase known as β phase with monoclinic crystal structure and $C2/c$ symmetry. Further, β-$Cu_2V_2O_7$ compound is a member of the family of transition-metal vanadium oxides $M_2V_2O_7$ (M = Cu, Ni, Co, Mn), which have attracted much interest due to their rich structural features and magnetic properties [14,17–25]. The α-$Cu_2V_2O_7$ compound is composed of magnetic $3d^9$ Cu^{2+} and a nonmagnetic $3d^0$ V^{5+} ions. The nonzero exchange couplings of Cu^{2+} ions interestingly forms both 1D zigzag chains due to strongest Cu-Cu exchange coupling as first

*akyogi@csr.res.in
†vasant@csr.res.in

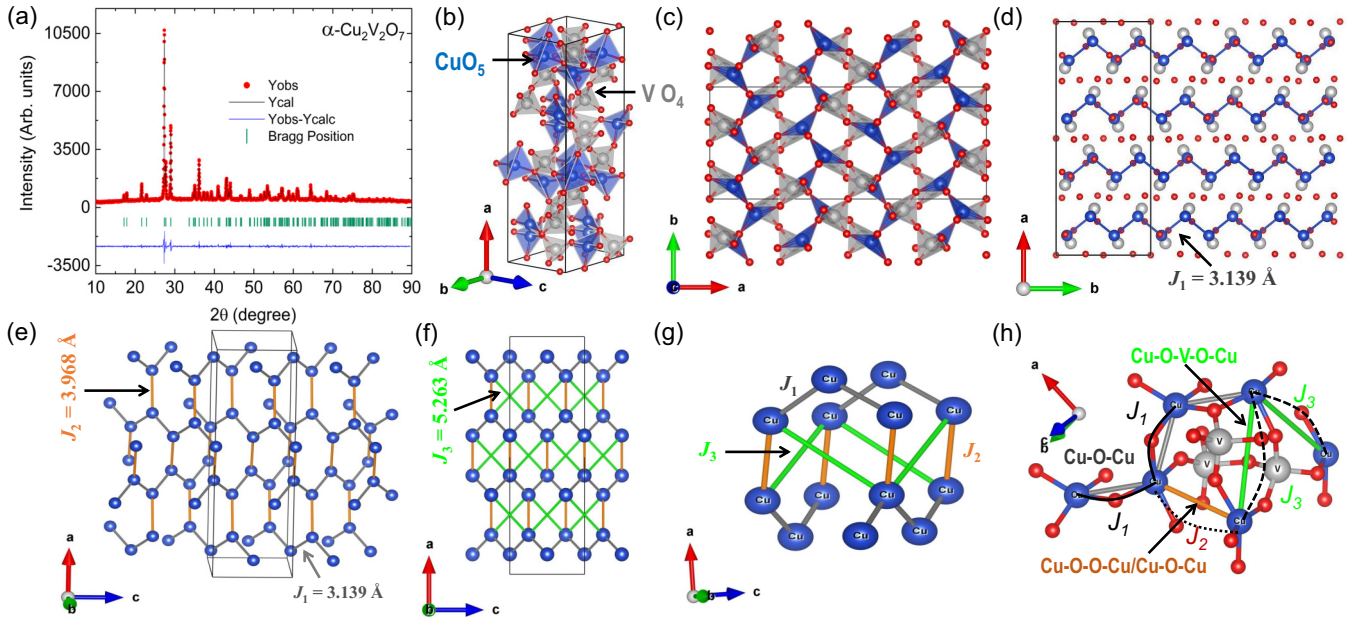

FIG. 1. (a) The room-temperature x-ray diffraction pattern for α-$Cu_2V_2O_7$ along with fitting carried out using Rietveld refinement. The observed and calculated patterns are shown by the filled circles and solid black lines, respectively. The difference between observed and calculated patterns is shown by the thin line at the bottom. The vertical bars are the theoretical Bragg peak positions for α-$Cu_2V_2O_7$. [(b), (c)] The crystal unit cell of α-$Cu_2V_2O_7$ having one copper (Cu) site, which forms local coordination CuO_5 (blue shaded pentahedral) and one vanadium (V) site, which forms local coordination as tetrahedral VO_4 (gray shaded) in the lattice. (d) The Cu^{2+} in the CuO_5 local environment forms zigzag chains by strong exchange coupling (J_1, NN) along the crystallographic direction [011]. (e) The two exchange couplings (J_1: NN and J_2: Second NN) in the unit cell forms quasi-2D helical-honeycomb network of Cu^{2+} spins for α-$Cu_2V_2O_7$ at room temperature. (f) Next-nearest-neighbors coupling (J_3: NNNs) also present coupled helical honeycomb. (g) The detailed view of coupled helical-honeycomb units in the *ac* plane, where J_3 can frustrate J_2 exchange interactions due to the presence of diagonal interaction between J_2 and J_3. (h) Different superexchange interactions present in the magnetic lattice.

NN ($J_1 = 3.139$ Å) along [011] direction and quasi-2D helical-honeycomb lattice arising from two Cu-Cu exchange couplings as second NN ($J_1 = 3.139$ Å and $J_2 = 3.968$ Å) in *ac* plane as shown in Figs. 1(d) and 1(e). In addition, the next-nearest-neighbor (NNNs as $J_3 = 5.263$ Å) interaction is present in the lattice and these interaction couples the helical-honeycomb lattice. The detailed view of coupled helical-honeycomb units in the *ac* plane is shown in Figs. 1(f) and 1(g). This NNNs exchange interactions J_3 can frustrate J_2 due to the presence of interdiagonal interaction between J_2 and J_3. However, the computed exchange interactions from inelastic neutron scattering (INS), density-functional theory (DFT), and quantum Monte Carlo (QMC) calculations suggested that dominant interactions are J_3 and the moment in α-$Cu_2V_2O_7$ compound is found to be along the crystallographic *a* axis [26]. Moreover, the 1D zigzag chains are running along the [011] direction [24–26]. Furthermore, neutron diffraction study showed that α-$Cu_2V_2O_7$ is an antiferromagnet with a weak ferromagnetism, which arises from the $3d^9$ Cu^{2+} spin canting due to the Dzyaloshinskii-Moriya (DM) interactions [24,25,27,28]. The neutron diffraction study also reveals a magnetically ordered state at $T_N = 33.4$ K with a small saturation magnetization of $\simeq 0.04$ μ_B [29].

The α-$Cu_2V_2O_7$ compound is a unique member in the family of pyrovanadates to have a noncentrosymmetric orthorhombic structure at room temperature. Cu ions arranged in the zigzag chains in [011] direction connected through two asymmmetric Cu-O-Cu bonds forming a noncentrosymmetric CuO_2 plaquette, which favors DM interaction as well as stabilizes the ferroelectric polarization. α-$Cu_2V_2O_7$ is an improper multiferroic system in which ferroelectric transition temperature (T_c) coincides with long-range magnetic ordering $T_N \sim 33.4$ K. It showed giant ferroelectric polarization of value 0.55 μC/cm^2 that is attributed to symmetric exchange striction mechanism. On applying very small magnetic field 0.9 T, dielectric permittivity value increases by 3.5% at $T_N \sim 33.4$ K. However, it shows sizable amount of magnetodielectric value up to 70 K. XRD study also illustrated change in volume below $T_N \sim 33.4$ K [22]. Further, INS reported by Banerjee *et al.* [24] related the observed broadening in the linewidth with the magnon-phonon scattering. This indirectly suggested strong spin-lattice coupling in this compound and thus may be the primary reason of multiferroic behavior shown by this compound. In addition, the temperature-dependent Raman spectroscopy and its detailed analysis across the magnetic transition can indirectly reveal the signature of existing magnetic ordering through spin-lattice coupling [30,31]. Raman scattering is a powerful and popular characterization tool to study spin-lattice coupling dynamics for both effective interaction between spins through lattice and additionally the impact of dimensionality onto magnetism. However, the lattice dynamics as well as experimental investigation of phonon structure and coupling among magnetic and lattice degrees of freedom is lacking in this compound.

Here, we investigate structural, vibrational, and field-induced thermodynamic properties of α-$Cu_2V_2O_7$ through

a combination of x-ray diffraction, magnetic susceptibility, specific heat, and Raman spectroscopy studies. We present a detailed Raman scattering measurements to explore its lattice vibrations and presence of spin-lattice coupling. The experimental result is also corroborated by the phonon calculations based on density-functional theory (DFT).

II. METHODS

The single-phase polycrystalline samples of α-$Cu_2V_2O_7$ compound is prepared by solid state method by firing stoichiometric mixtures of high pure CuO (99.999%, Aldich), and V_2O_5 (99.999%, Alfa Aesar) at 550°C for 24 h and subsequently at 650°C for 48 h. The progress of the reaction was followed by powder x-ray diffraction (P-XRD). To ensure the purity of the sample, P-XRD (Bruker powder diffractometer and CuK_α radiation, $\lambda = 1.54182$ Å) was performed at room temperature. The measured diffraction patterns were analyzed by Rietveld refinement using Fullprof suite program [32]. Magnetic susceptibility $\chi(T)$ measurements were performed using MPMS SQUID-VSM (Quantum Design) and heat capacity $C_p(T)$ measurements were performed using a commercial Physical Property Measurement System (PPMS, Quantum Design). Raman measurements were recorded by using a Horiba JY HR-800 spectrometer equipped with 1800 g/mm grating and a charge-coupled device detector. We used He-Ne laser (633 nm) as an excitation source, which was focused onto ∼2 μm [50x objective [numerical aperture (NA) = 0.50] diameter spot in the backscattering geometry. The incident laser power was ∼3 mW for 633 nm excitation. Prior to the measurement the Raman instrument was calibrated by the peak position of single crystal of α-Si(111) substrate. The chemical valence state of the elements present in α-$Cu_2V_2O_7$ were investigated by x-ray absorption spectroscopy (XAS) and x-ray photoelectron spectroscopy (XPS). XPS experiments were conducted using an Al K_α ($h\nu$ = 1486.7 eV) laboratory source and hemispherical energy analyzer (Omicron, EA-125, Germany) at angle integrated photoemission spectroscopy (AIPES) beamline (Indus-1, BL 2, RRCAT, Indore, India). XAS experiment was carried out with an experimental resolution of 0.25 eV in the total electron yield mode at beamline BL-01, Indus 2 synchrotron source at RRCAT, Indore, India.

The DFT calculations were performed using Vienna based ab-initio simulation package (VASP) [33–35]. Projected augmented wave (PAW) flavor of pseudopotential within generalized gradient approximation (GGA) parametrization by Perdew, Burke, and Ernzerhof [36,37] with kinetic energy cutoff of 600 eV is used. To integrate the Brillouin zone a 134 k-point mesh was generated using Monkhorst-Pack method [38] and a convergence criterion of 10^{-3} eV $Å^{-1}$ and 10^{-8} eV were chosen for ionic forces and total energy, respectively to ensure to convergence of less than 0.1 meV in total energy for precise calculation of phonons. We performed both non-spin-polarized and collinear spin-polarized calculations. The magnetic calculations have been carried out for the G-type antiferromagnetic ordering in the *Fdd2* phase. The zone center phonon calculations were performed using density functional perturbation method as implemented in VASP.

TABLE I. Fractional atomic coordinates obtained from Rietveld refinement of XRD pattern of α-$Cu_2V_2O_7$ at room temperature, the site occupancies (Occ.) and isotropic thermal parameters (B_{iso}) were kept constant. The goodness of fit, $\chi^2 = 1.9$.

Atom	Site	x/a	y/b	z/c	B_{iso}	Occ.
Cu1	16*b*	0.1662(3)	0.3650(12)	0.750(14)	0.0	1.0
V1	16*b*	0.1995(3)	0.4063(15)	0.2328(18)	0.0	1.0
O1	16*b*	0.1616(6)	0.3479(4)	0.4500(4)	0.0	1.0
O2	16*b*	0.2449(5)	0.5611(3)	0.2700(3)	0.0	1.0
O3	16*b*	0.1447(10)	0.4363(5)	0.0290(6)	0.0	1.0
O4	8*a*	0.2500(0)	0.2500(0)	0.1620(3)	0.0	1.0

III. RESULTS

A. Powder x-ray diffraction and crystallography

Sample quality was checked by powder x-ray diffraction and no impurity phases were found in α-$Cu_2V_2O_7$. The Rietveld refinement of the room-temperature x-ray diffraction pattern [Fig. 1(a)] confirms that as synthesized α-$Cu_2V_2O_7$ compound crystallizes in an orthorhombic crystal structure with noncentrosymmetric space group $Fdd2$ (space group No. 43). Refined lattice parameters are $a = 20.680\,(5)$ Å, $b = 8.405\,(12)$ Å, and $c = 6.450\,(10)$ Å. These lattice parameter values agree well with the values reported by Calvo *et al.* [14]. The refined values of various structural parameters such as fractional atomic coordinates, and isotropic thermal parameters are given in Table I for α-$Cu_2V_2O_7$. All atoms occupy at the Wycoff sites 16 *b* and 8 *a* and all the atomic sites are found to be fully occupied. The crystal structure of α-$Cu_2V_2O_7$ compound is composed of two different types of Cu^{2+} zigzag chains [Fig. 1(c)], which are mutually perpendicular along with strong interchain exchange interactions. The interchain interactions between Cu^{2+} atoms are forming helical-honeycomb lattice [Fig. 1(d)] in crystallographic *ac* plane [24,25].

Furthermore, the magnetic lattice in α-$Cu_2V_2O_7$ is defined by two types of geometrical arrangements of Cu^{2+} ions having the first NN exchange interactions ($J_1 \simeq 3.139$ Å) via Cu-O-Cu and it forms quasi-1D zigzag spin chains running along the crystallographic direction of [011]. The second NN interaction ($J_2 \simeq 3.968$ Å) arises due to Cu-O-Cu superexchange bridge as shown in Fig. 1(d). The J_1 and J_2 forms a quasi 2D helical-honeycomb lattice geometry in *ac* plane as shown in Fig. 1(d) [24,25]. The 1D chain and quasi 2D helical-honeycomb lattice geometry are formed by the corner sharing polyhedra of CuO_5 pyramids and VO_4 tetrahedra in α-$Cu_2V_2O_7$ [Fig. 1(b)]. Along the *b* axis much weaker interactions are expected as the distances between chains are quite longer. A schematic exchange coupling of coupled zigzag chains and helical honeycomb in α-$Cu_2V_2O_7$ is shown in Figs. 1(e) and 1(f) where J_1 and J_2 are the exchange interactions.

B. Magnetic susceptibility and magnetization

The magnetic susceptibility $\chi(T)$ data for α-$Cu_2V_2O_7$ measured at an applied magnetic field $H = 1$ T is presented in Fig. 2(a). At high temperatures $T > 75$ K, $\chi(T)$

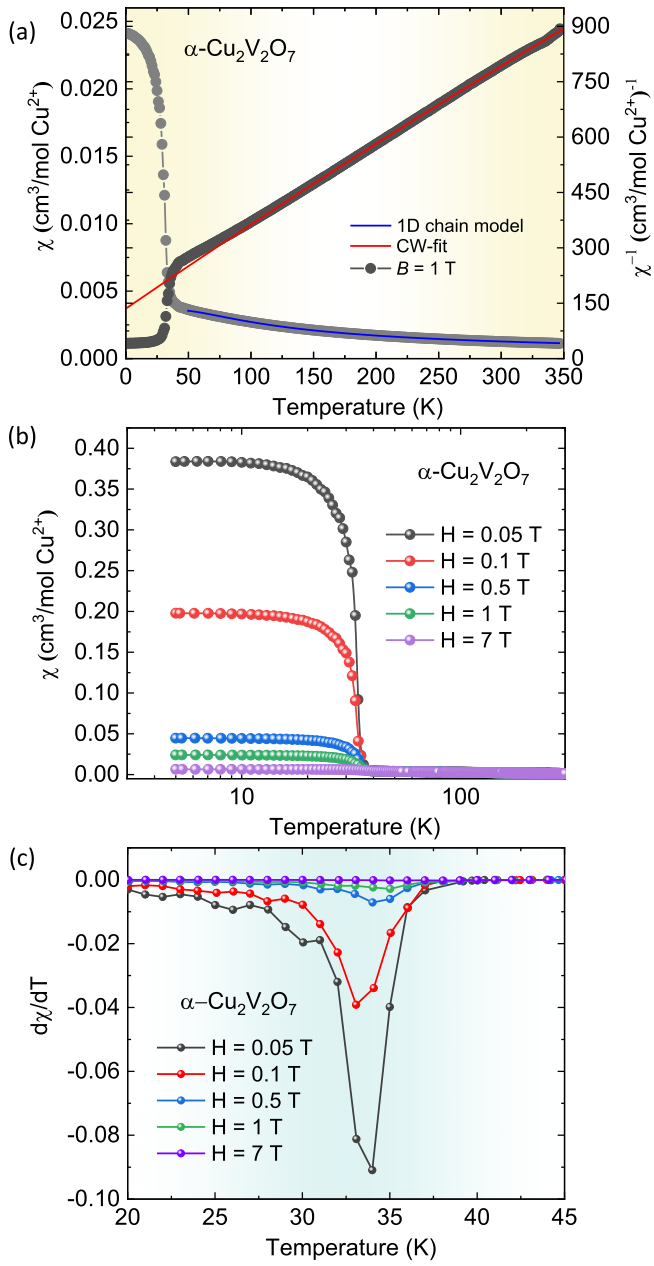

FIG. 2. (a) The magnetic susceptibility $\chi(T)$ of α-$Cu_2V_2O_7$ under an applied magnetic field of $H = 1$ T. The solid thick blue line is the fit as per the 1D Heisenberg spin-1/2 chain model as discussed in text (left axis). The inverse dc-magnetic susceptibility $\chi^{-1}(T)$ of α-$Cu_2V_2O_7$ measured under an applied magnetic field of $H = 1$ T (right axis). The straight solid red line is the linear fit to the $\chi^{-1}(T)$ data above 75 K. The *dc*-magnetic susceptibility $\chi(T)$ of α-$Cu_2V_2O_7$ (b) and its derivative (c) measured under several applied magnetic fields $H = 0.05$, 0.1, 1, and 7 T.

follows a Curie-Weiss law. The susceptibility increases with decreasing temperature, while a sharp long-range ordered (LRO) transition is observed at 33.4 K, indicating the onset of AFM ordering as shown in the Fig. 2(c) by the derivative of susceptibility, which is characteristic of LRO. The magnetic properties and the transition observed for α-$Cu_2V_2O_7$ are different from those of β and γ phases [14,17,39]. The β-$Cu_2V_2O_7$ phase is a 2D planner honeycomb lattice system in which the magnetism can be described as a spin-$\frac{1}{2}$ Heisenberg system. However, the α-$Cu_2V_2O_7$ phase is better described by two sets of mutually perpendicular zigzag chains with reasonably strong NN and sizable NNN interchain exchange interactions. Here, we have tested of 1D antiferromagnetic nature by fitting of temperature-dependent magnetic susceptibility using 1D spin-$\frac{1}{2}$ Bonner-Fisher model [40]. The temperature-dependent susceptibility curve of α-$Cu_2V_2O_7$, is well accounted by an AFM spin-$\frac{1}{2}$ chain model (Bonner-Fisher model [40]) with an exchange coupling of ∼62.13 K (∼5.35 meV) and the g value of ∼1.94 as shown by solid blue line (above 50 K) in the Fig. 2(a). The first-nearest-neighbor interaction J_1 (J_{intra}) obtained from the fit of magnetic susceptibility is ∼5.35 meV, which is in good agreement with DFT calculations [29]. Furthermore, the interchain exchange interaction J_2 in quasi-1D lattice can be estimate using the Schulz's calculation under the mean-field (MF) approximation [41]. The expression for estimation of 1D interchain exchange interaction J_2 can be given as

$$J_2 = T_N/(1.28 \times \sqrt{(\ln(5.8 \times J_{\text{intra}})/T_N)}), \tag{1}$$

From Eq. (1) we have estimated the interchain interactions in α-$Cu_2V_2O_7$, which is found to be $J_2 \sim 16.91$ K for the mutually parallel chains under the MF approximation. The actual sign of magnetic exchange coupling at the MF level can be +ve (FM) or–ve (AFM) as these properties are determined by the mean of interchain exchange coupling constant [41]. Calculated values of exchange coupling J_1 and J_2 from the magnetization data are compared with the INS, QMC, and DFT calculations obtained exchange couplings have been listed in the Table V (see below). Moreover, we have calculated the ratio of the intrachain and inter-chain interaction i.e. $J_2/J_{\text{intra}} \simeq 0.272$, which is relatively much larger than that found in quasi one-dimensional $BaCu_2Si_2O_7$ ($J_2/J_{\text{intra}} \simeq 0.011$) [42]. The mean-field analysis indicates a less pronounced 1D and significant 2D character (J_1 and J_2) is present in α-$Cu_2V_2O_7$. Further, we have also confirmed the susceptibility data by fitting with different dimensionality describing 2D magnetic-lattices as triangular- and square-lattice spin models [43–46], which are used for fitting the T-dependent susceptibility (for details, see Sec. II along with Figs. S9 and S10 within the Supplemental Material [47]). Therefore, the magnetic lattice can be better explain by considering a mixed dimensionality in α-$Cu_2V_2O_7$.

In addition to this, a typical Curie-Weiss behavior is observed above 75 K in the $\chi^{-1}(T)$ for α-$Cu_2V_2O_7$, as shown in the Fig. 2(a) (right axis) . From the Curie-Weiss fitting Eq. (2), Curie constant C and the Weiss constant θ_{CW} was obtained,

$$\chi = \chi_0 + \frac{C}{T - \theta_{\text{CW}}}, \tag{2}$$

where χ_0 is the temperature-independent contribution that accounts for core electron diamagnetism and Van Vleck (VV) paramagnetism. The second term is the Curie-Weiss (CW) law with Curie constant C ($= N_A\mu_{\text{eff}}^2/3k_B$, where N_A is Avogadro's number, μ_{eff} is the effective magnetic moment, and k_B is Boltzmann's constant) and Weiss temperature θ_{CW}. The data above 75 K were fitted with the parameters $\chi_0 = 8.690\,(5) \times 10^{-5}$ cm^3/mol Cu, $C = 0.420\,(3)$ cm^3 K/mol

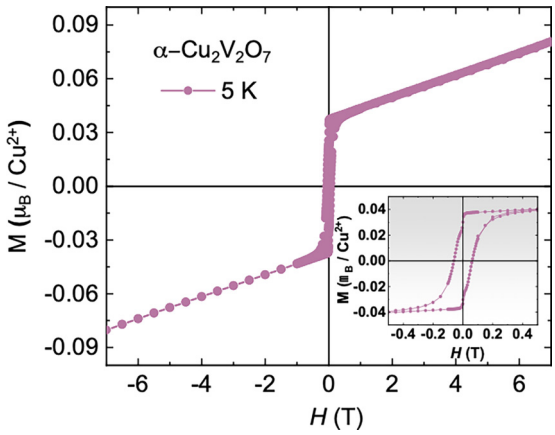

FIG. 3. Magnetization as a function of applied field (H) measured at 5 K. The inset shows zoomed view of M(H) depicting weak magnetic hysteresis loops.

Cu, and $\theta_{CW} = -57.56\,(8)$ K. The effective magnetic moment μ_{eff} is calculated to be 1.83 (2) μ_B, which is in good agreement with the Cu^{2+} ions for a $S = \frac{1}{2}$ and a g value of 2 (free-electron g value). The negative Weiss constant suggests that the dominant interactions between Cu^{+2} ions are AFM. The temperature-dependent magnetic susceptibility $\chi(T)$ data for α-$Cu_2V_2O_7$ measured as a function of temperature under different applied fields are shown in the Fig. 2(b) and there derivative are plotted in the Fig. 2(c). The temperature-dependent susceptibility derivatives $\partial(\chi)/\partial T$ versus T curve at various fields clearly indicating LRO at $T_N = 33.4$ K at lower field. The $\chi(T)$ shows suppression on increasing magnetic field, which is attributed to decreasing in spin canting angle.

Moreover, in order to further confirm the AFM correlation and also to check about the existence of any field-induced effect at low temperature, we measured M(H) below the ordering temperature $T_N = 33.4$ K. The isothermal magnetization curve M(H) measured over all four quadrants below the LRO at 5 K is shown in Fig. 3. A week ferromagnetic hysteresis with a coercive field of the order of ∼0.05 T and a remnant moment of the order of ∼0.035 μ_B is evident. This is not related to any weak ferromagnetic impurity at low temperature present in the sample, rather, the 1D chains of Cu^{2+} spins are having canted angel as experimentally found in neutron study indicating the presence of the finite Dzyaloshinskii-Moriya (DM) interaction in α-$Cu_2V_2O_7$ [24,25,27,28]. The weak hysteresis loop and the resulting coercivity field is in good agreement with the observed weak ferromagnetism with small saturation magnetization of ≃0.035 μ_B below LRO as shown in the inset of the Fig. 3. Further, the linear change of magnetization with field is indicative of a characteristic AFM ground state. The M(H) curve did not show any sign of saturation even at (H_s ∼ 7 T) as well as spin-flop transition could not be observed at 6.5 T due to powder averaging effect [25]. However, the value of magnetization at 7 T (M_{7T} ∼ 0.08 μ_B/Cu^{2+}) is quite far than the theoretically expected saturation magnetic moment of $M_s = gS\mu_B = 1$ μ_B/Cu^{2+} ($S = \frac{1}{2}$); this indicates that the saturation field H_s is probably very high. There is a slow linear increase in M(H) curve that is attributed to the temperature-independent Van-Vleck paramagnetic contribution, typical for a Cu^{2+} ion in a CuO_5 environment [48].

C. Heat capacity

The low-T specific heat $C_p(T)$ measured using the thermal-relaxation technique as a function of temperature at zero field is presented in Fig. 4(a). At high temperatures, C_p is completely dominated by phonon excitations [49,50]. Below 33.4 K, an increase of C_p with decreasing temperature indicates that the magnetic contribution of specific heat is dominant in this temperature region. Here, $C_p(T)$ shows a λ-type anomaly at $T_N \simeq 33.4$ K associated with the long-range magnetic ordering in α-$Cu_2V_2O_7$ [see Fig. 4(a)], which is in good agreement with the magnetization results. Below T_N, $C_p(T)$ decreases gradually towards zero.

In order to estimate the phonon part of the heat capacity $C_{ph}(T)$ in α-$Cu_2V_2O_7$, the $C_p(T)$ data at high temperature were fitted by a single Debye contributions. The Debye-type heat capacity is given by

$$C_D(T) = 9R(T/\Theta_D)^3 \int_0^{\Theta_D/T} \frac{x^4 \exp(x)}{(\exp(x)-1)^2} dx, \qquad (3)$$

where θ_D is characteristic Debye temperature. In order to simplify the fit procedure, a Padé approximant for the Debye-type heat capacity, proposed recently by Goetsch *et al.* [51], was utilized. The Debye fit is used to extract the phonon contribution and it has been adopted for various condensed matter systems [49,51–53]. Figure 4(a) shows the fit of $C_{ph}(T)$ by Eq. (3) (solid red line) resulting in Debye temperature $\theta_D \simeq 449$ K. Finally, the high-T fit was extrapolated down to 2 K and $C_{mag}(T)$ was estimated by subtracting $C_{ph}(T)$ from $C_p(T)$ as shown by blue solid line in the Fig. 4(a).

The magnetic part $C_{mag}(T)$ verified by integrating $C_{mag}(T)/T$ to estimate the magnetic entropy is found to be $S_{mag} \simeq 41$ J/mol K at 150 K. This is significantly higher from the pure magnetic entropy as $S_{mag} = 2\text{Rln } 2 \simeq 11.5$ J/mol K expected for spin-$\frac{1}{2}$ [Fig. 4(b)]. Enhanced value of $S_{mag} \simeq 30$ J/mol K was reported by Wang *et al.* [54]. Such a high value of S_{mag} can be because of multiferroic nature of α-$Cu_2V_2O_7$ and strong magnetolattice coupling, which is not investigated so far. In order to gain additional insight into the nature of magnetic heat capacity we use power law for the analysis. We examine the C_{mag} well below T_N in terms of the spin-wave (SW) contribution to the heat capacity of α-$Cu_2V_2O_7$. At low temperatures the heat capacity follows a power law due to magnon excitations [50], which can be describe by the following equation:

$$C_{mag}(T) \propto T^{d/n}, \qquad (4)$$

where d is the dimensionality of the magnetic lattice and $n = 1$ for AFM and $n = 2$ for FM magnons. To evaluate dimensionality of the magnetic lattice present in this compound, we have fitted the curve using Eq. (4) by taking different dimension ($d = 1, 2, 3$). An attempt is made to fit the curve by letting d as variable, which resulted in $d = 1.83$. As seen from Fig. 4(c), the curve can be well fitted using Eq. (4) at low temperature [49,51–53]. It quantitatively agrees well with the observations of mean field analysis as extracted from the magnetization results. A reasonable fit resulted for $d = 1, 2$

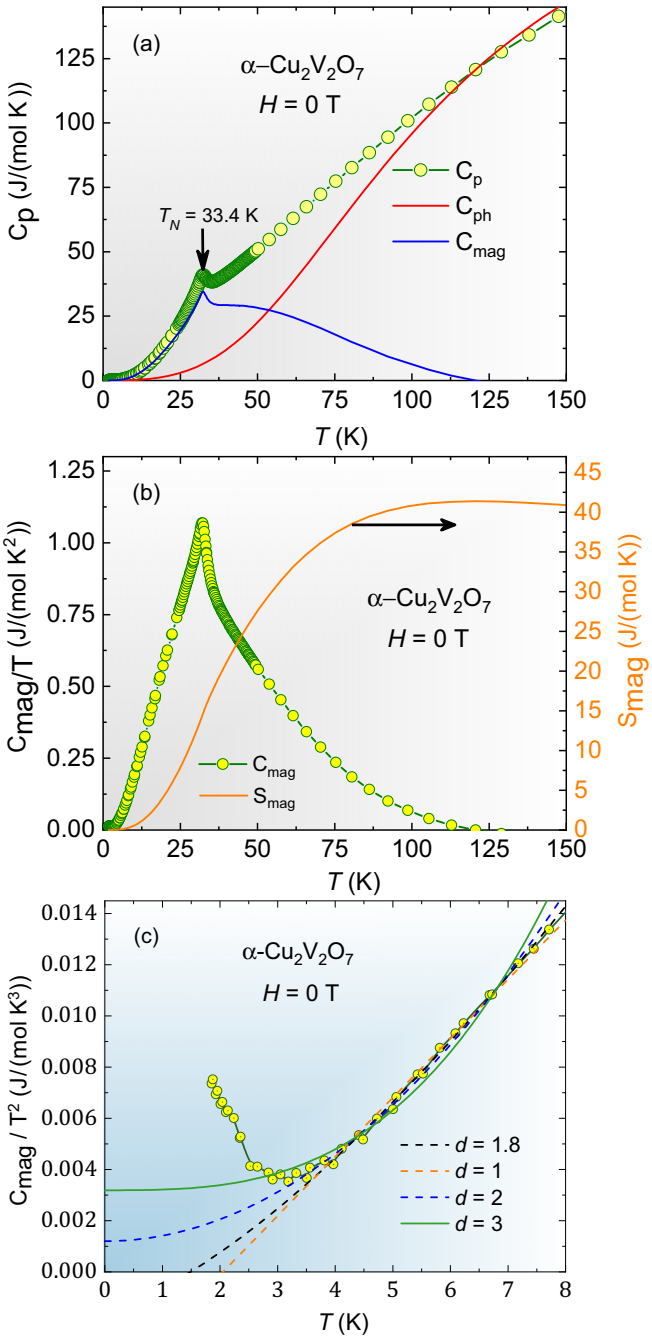

FIG. 4. (a) Temperature dependence of the specific heat C_p of α-$Cu_2V_2O_7$ measured under zero field. Open circles are the experimental data (α-$Cu_2V_2O_7$), the solid red line shows the phonon contribution C_{ph} estimated from the Debye model fit, and the solid blue line indicates the magnetic contribution ($C_{\rm mag}$). (b) The $C_{\rm mag}/T$ as a function of temperature over the low temperature range (2–150 K). The calculated magnetic entropy ($S_{\rm mag}$) (solid orange line) as a function of temperature is plotted in the right axis. (c) The low-temperature $C_{\rm mag}/T^2$ as a function of temperature represented by open filled circles fitted using Eq. (4) for various d values.

and $d = 1.83$ while the fit was found to be poor for $d = 3$, indicating quasi 2D type magnetic lattice and AFM magnon excitation at low temperature rather than 3D type magnetic lattice. The best fit χ^2 values for various d are shown in Table

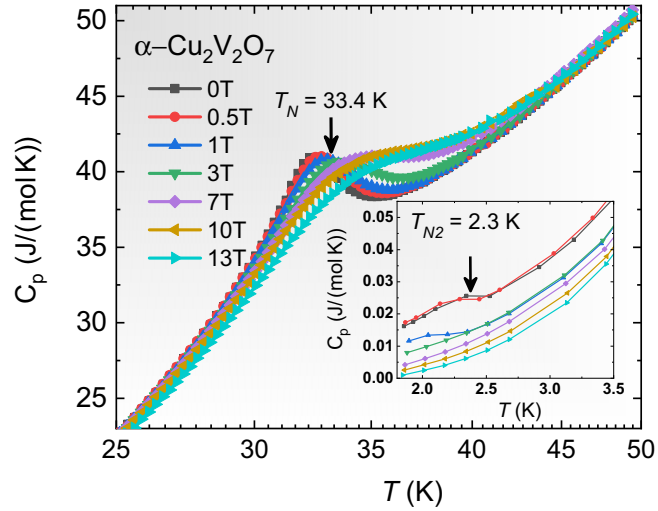

FIG. 5. Heat capacity of of α-$Cu_2V_2O_7$ measured under different applied magnetic fields. The low-field (zero-field) data shows λ-type anomaly at $T_{\rm N} \simeq 33.4$ K as shown by a downward arrow. The inset of the figure provide zoomed view at low temperature showing an additional new feature, which may be related to the another magnetic transitions at $T_{\rm N2} = 2.3$ K marked by the downward arrow.

S1 within the Supplemental Material [47], which is found to be best for 1 and 1.83, respectively. Moreover, the low temperature pronounced upturn is observed in $C_{\rm mag}/T^2$ as a function of temperature around 2.3 K, indicating the possibilities of magnetic ordering is discussed below.

To gain further information about the nature of magnetic ordering under an applied magnetic fields, we have measured $C_{\rm p}(T)$ under different applied magnetic fields as shown in Fig. 5. With increasing H from 0 T to 13 T, the λ-type anomaly broadens after certain applied field ($H \leqslant 7$ T). This indicates presence of magnetolattice coupling and multiferroic behavior of this compound. Moreover, in our low-temperature heat capacity data, an additional feature is observed, which may be related to the another magnetic ordering transition at $T_{\rm N2} = 2.3$ K as shown by the downward arrow in the inset of the Fig. 5. This new low-temperature magnetic transition anomaly at $T_{\rm N2} = 2.3$ K is slightly shifting towards lower temperature and it fully suppressed at an applied field of $H \approx 3$ T as shown in the inset of the Fig. 5. Similar type of the low-temperature double AFM magnetic transition have been observed in other magnetic materials [55,56].

D. XAS and XPS

We have performed x-ray absorption near edge spectroscopy (XANES) for α-$Cu_2V_2O_7$, which is a local probe and can reveal crucial informations like oxidation state, coordination numbers of the absorbing atoms. One of the important part for α-$Cu_2V_2O_7$ compound is to check the presence of Cu^{2+} oxidation state and for the same we have measured XANES at room temperature. The V $L_{3,2}$, Cu $L_{3,2}$ edge spectrum along with iso-electronic CuO and V_2O_5 samples were also measured at room temperature and shown in Figs. 6(a) and 6(b) respectively. The V L-edge spectra consists of two distinct peaks at 518 eV and 525 eV assigned to L_3 (V $2p_{3/2}$ -

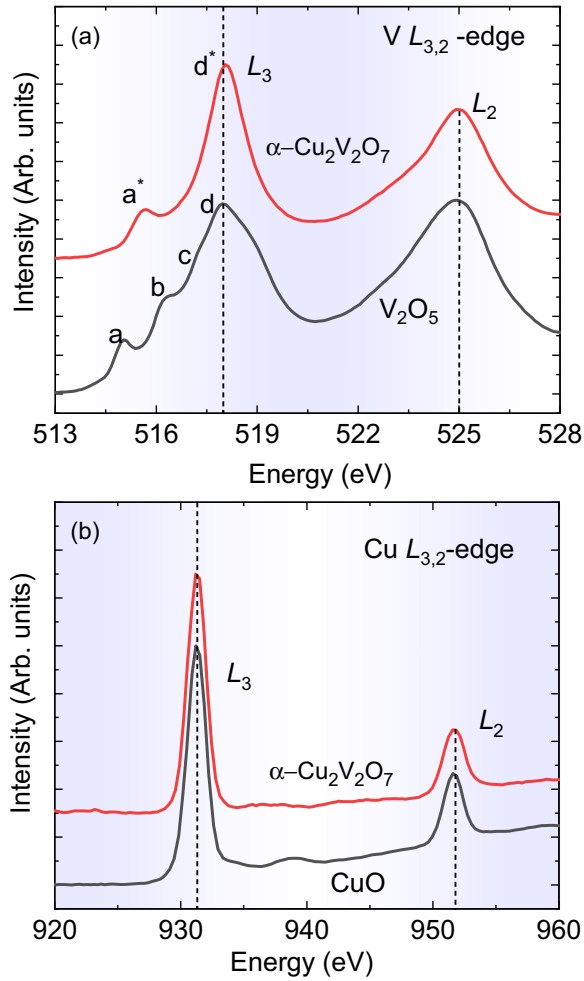

FIG. 6. The V $L_{3,2}$-edges x-ray absorption near edge spectrum (XANES) at room temperature (a) and Cu $L_{3,2}$-edges (b) spectrum of the α-$Cu_2V_2O_7$ along with the V_2O_5 and CuO as reference sample, respectively.

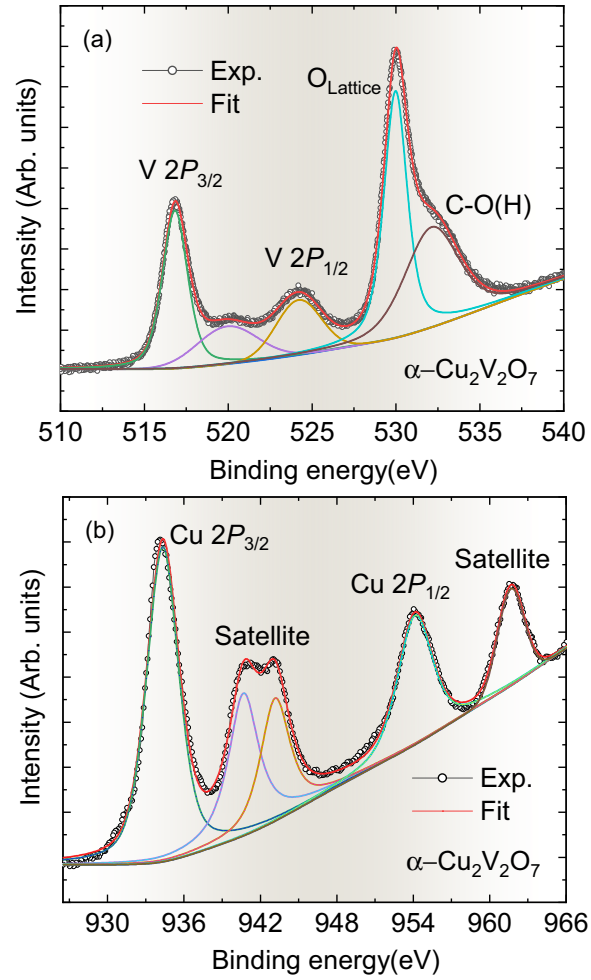

FIG. 7. The deconvoluted V $2p_{3/2}$ and O 1*s* (a) and Cu $2p_{3/2}$ (b) core level x-ray photoelectron spectrum (XPS) of α-$Cu_2V_2O_7$.

3*d*) and L_2 (V $2p_{3/2}$ - 3*d*) edges, respectively. The Position of V L_3 and V L_2 matches well with the reference V_2O_5 sample, which confirms V^{5+} valence state [57,58] in the α-$Cu_2V_2O_7$ compound. Furthermore, the Cu L_3, L_2 peaks were emerged due to the electronic transition of Cu $2p_{3/2}$ to 3*d* interbands at position 931.2 and 951.8 eV, respectively. The position and the intensity ratio of Cu L_3: Cu L_2 is found to be very much similar with reference CuO as shown in the Fig. 6(b), indicating that the Cu is in Cu^{2+} valence state in α-$Cu_2V_2O_7$ [59,60]. Interestingly, pre-edge structure at V L_3 edge is found to be drastically different in α-$Cu_2V_2O_7$ compound when compared to V_2O_5. The peak at *a*, *b*, *c* are absent in case of α-$Cu_2V_2O_7$ and a feature a^* at 515.6 eV is only evident as shown in the Fig. 6(a). This is due to different crystal electric field (CEF) and local structure in α-$Cu_2V_2O_7$ compound as compared to V_2O_5. The peak at a^* is arising due to the transition between V $2p_{3/2}$ to $3d_{xy,yz,xz}$ and the peak at d^* is arising due to the transition between V $2p_{3/2}$ to $3d_{x^2-y^2,z^2}$. further, the V L_2-edge is broadened than that of V L_3 edge by a Coster-Kronig Auger decay process into a $2p_{3/2}$ hole [61].

In addition, to check the chemical valence-sates, the core level spectra of copper (Cu), vanadium (V) and oxygen (O) have been studied by x-ray photoemission spectroscopy (XPS). Figures 7(a) and 7(b) show the V 2*p*, O 1*s*, and Cu 2*p*, core level photoemission spectra of α-$Cu_2V_2O_7$. The core-level spectrum was fitted with a combination of the Lorentzian and Gaussian functions to estimate the position of individual features. The background of the spectrum is corrected by the Tougaard inelastic method. The binding energy position of V $2p_{3/2}$ and V $2p_{1/2}$ are found to be 516.8 and 524.3 eV respectively, with separation 7.5 eV as shown in the Fig. 7(a). The separation is due to spin-orbit-coupling (SOC) interaction, also confirms V^{5+} as a valence state in α-$Cu_2V_2O_7$ [62–64]. The peak at 520.3 eV is due to an x-ray satellite of Al $K_{\alpha 3}$ source [65]. Moreover, the O 1*s* peak at 530 eV is seen, which is lattice oxygen in α-$Cu_2V_2O_7$. An additional feature at 532.3 eV as shown in the Fig. 7(a) is related to the chemically adsorbed oxygen in the form of C-O(H). Similarly, the fitted binding energy (BE) positions of Cu $2p_{3/2}$ and Cu $2p_{1/2}$ are 933.2 and 953.2 eV, respectively as shown in the Fig. 7(b), it is splitted by 20 eV due to the SOC interaction. This further confirms the presence of Cu^{2+} in the α-$Cu_2V_2O_7$ [66,67]. Two strong satellite peaks (941.3 and 943.7 eV) in the

TABLE II. The factor-group method is used for the calculation of the symmetry properties, and the selection rules as per the orthorhombic crystal structure with space group $Fdd2$ (space group No. 43) for all types of vibrational modes of α-$Cu_2V_2O_7$. The factor group analysis of total number of phonon modes are listed for α-$Cu_2V_2O_7$.

Atom mode	Wycoff position	Mode decomposition Raman active mode + IR active
Cu1	16*b*	$(3A_1 + 3B_1 + 3B_2)_{R,IR} + (3A_2)_R$
V1	16*b*	$(3A_1 + 3B_1 + 3B_2)_{R,IR} + (3A_2)_R$
O1	16*b*	$(3A_1 + 3B_1 + 3B_2)_{R,IR} + (3A_2)_R$
O2	16*b*	$(3A_1 + 3B_1 + 3B_2)_{R,IR} + (3A_2)_R$
O3	16*b*	$(3A_1 + 3B_1 + 3B_2)_{R,IR} + (3A_2)_R$
O4	8*a*	$(A_1 + 2B_1 + 2B_2)_{R,IR} + (A_2)_R$
$\Gamma_{total} = 16\ A_1 + 16\ A_2 + 17B_1 + 17B_2$		

higher binding energy side of Cu $2p_{3/2}$ and one satellite peak (962.1 eV) of Cu $2p_{1/2}$ peak are the characteristics of Cu^{2+} valance charge state [68].

E. Raman scattering

1. DFT calculations

The factor group analysis of the α-$Cu_2V_2O_7$ is carried out. It is noted that the Raman spectra acquired in a backscattering geometry is a first-order process related to phonons present at the Brillouin zone center. According to factor group analysis the irreducible representation of the zone center modes resulted in 66 modes containing Raman, IR and silent modes as $\Gamma_{total} = 16A_1 + 16A_2 + 17B_1 + 17B_2$, which are listed in Table II. First-principles calculations based on density functional theory (DFT) have been applied successfully for extracting both IR and Raman active phonon modes. The phonon calculations were done using DFT and the assignment of IR and Raman active phonon modes were done using the calculated eigenvector symmetry for a mixed dimensionality lattice α-$Cu_2V_2O_7$. The predicted total IR and Raman active modes are listed in the Table II. The position of Raman active phonon modes as predicated using DFT along with experimentally observed position of Raman phonon mode at room temperature are listed in Table III. Moreover, the theoretical values elucidated from DFT is reasonably in good agreement with the experimentally observed values at room-temperature (Table III). The eigen displacement vector along various crystallographic direction and planes are shown in Supplemental Material [47]. The eigen displacement vectors have been calculated by DFT for different oxygen, vanadium and copper atoms along with various polyhedral local environment distortion [CuO_5 and VO_4] of the Raman and Infrared active modes are presented (for details, see Figs. S1–S8 within the Supplemental Material [47]).

2. Temperature-dependent Raman spectroscopy

The Raman spectra of α-$Cu_2V_2O_7$, acquired using excitation wavelength $\lambda_{exc} = 633$ nm at different temperatures is illustrated in Fig. 8. To understand the spin-lattice dynamics present in the compound, we performed the detailed temperature-dependent Raman spectroscopy in the temperature range from 3.5 K to 300 K. Experimentally, at room temperature, a total of 18 Raman modes are detected. Further, we have fitted all the Raman spectrum by Lorentzian function and obtained mode position and FWHM of all observed modes. All the experimentally obtained Raman modes have been labeled as R_0 to R_{17}. The Raman mode frequency showed an anomalous change as a function of temperature at and above T_N. The evolution of Raman mode frequency as a function of temperature for selected Raman modes is plotted as contour plots in Figs. 8(b) and 8(e). The intensity of the Raman mode is represented by color code. It is observed that for some modes the anomalous change is at $T_N \simeq 33.4$ K while for many it is well above T_N. These modes showed softening upon decreasing temperature below 50 K. The T_{SRO} is depicted by a closed circle in Figs. 8(b)–8(e). The Raman shift and FWHM of the various modes as a function of temperature is plotted in Fig. 9. It is clearly evident from our experiments over α-$Cu_2V_2O_7$ compound that most of Raman modes (R_2 R_3, R_8 R_{10}, R_{14}, R_{15} modes) showed a softening below 50 K well above the long-range antiferromagnetic ordering ($T_N \simeq 33.4$ K). Generally softening below magnetic ordering temperature is related to spin-phonon coupling [30,31,69,70]. The mode softening below 50 K thus most probably related to the occurrence of the short-range ordering (T_{SRO}) in α-$Cu_2V_2O_7$, and it is also consistent with the earlier study of magneto-dielectric and inelastic neutron study on this compound [22,24]. The FWHM of various modes also showed anomalous changes below 50 K establishing spin-lattice coupling in this system.

Furthermore, to explain the spin-phonon coupling behavior below the magnetic transition temperature in α-$Cu_2V_2O_7$, we have calculated phonon frequency and spin-phonon coupling coefficient of each of the Raman modes. For this purpose, the change in the phonon frequency can be written as

$$(\Delta\omega)_{\text{Total}} = (\Delta\omega)_{\text{Latt.}} + (\Delta\omega)_{\text{Mag.}} + (\Delta\omega)_{e-ph} \quad (5)$$

where ω is the Raman phonon frequency. In the first term, change in phonon frequency arises due to lattice contribution originating from anharmonicity. It is noted that α-$Cu_2V_2O_7$ does not shows any structural change in temperature range 3.5 K to 300 K. Thus, as temperature rises, atomic equilibrium positions and interatomic forces change, causing thermal expansion due to anharmonicity. The second term represents the change in phonon frequency due to spin-phonon coupling. In third term, frequency modulation arises due to

TABLE III. The position of phonon modes [Raman mode (R) and infrared active mode (IR)] predicated by DFT along with experimentally observed position of Raman modes at room temperature (300 K).

Mode	Exp. (cm^{-1})	Symmetry	Cal. (cm^{-1})	Vibration
R_0	147.69	B_2	149.28	Cu-O_1-V bending mode.
R_1	166.79	B_2	162.00	CuO_5 distortion via O_1 and O_2 displacement.
		A_1	165.76	In phase O_3 displacement along *a* axis.
R_2	175.05	A_1	174.67	VO_4 distortion via O_3 and O_2 displacement.
		A_2	178.16	CuO_5 distortion.
R_3	208.10	A_2	201.26	CuO_5 distortion.
		A_1	202.28	CuO_5 bending distortion.
		A_2	204.57	CuO_5 distortion via O_2 and O_3 displacement.
R_4	245.18	B_1	233.79	In phase O_1 displacement along *a* axis.
		A_2	239.39	In phase O_1, O_2 and O_3 displacement along *a* axis.
		B_2	250.83	Out of phase O_3 displacement along *a* axis.
		B_2	263.04	Out of phase O_1 displacement along *a* axis.
		A_1	267.02	CuO_5 rotation around a axis.
R_5	292.67	A_2	276.41	CuO_5 distortion via O_2 and O_3 displacement.
		A_2	286.11	CuO_5 distortion via O_1, O_2 and O_3 displacement.
		B_1	289.15	O_4 and O_2 relative displacement along *a* axis.
		B_1	304.32	O_1 and O_3 displacement along *a* axis.
R_6	318.73	B_2	313.38	O_4 and O_2 relative displacement in *ab* plane.
		A_2	315.67	CuO_5 distortion via O_1, O_2 and O_3 displacement.
R_7	326.92	B_1	336.65	O_3 and O_2 displacement in *ac* plane.
		B_2	338.78	CuO_5 distortion via O_1, O_2 and O_3 displacement.
		A_1	341.78	VO_4 tetrahedral distortion via O_1, O_2, O_3 andO_4 displacement.
R_8	357.09	A_2	345.02	VO_4 tetrahedral distortion via O_2 and O_4 displacement.
		A_1	353.29	O_1 and O_3 relative vibration along *a* axis.
		B_1	363.80	O_2 and O_4 relative vibration along *a* axis.
R_9	376.08	B_2	383.18	O_1, O_2 and O_3 andO_4 displacement along a axis.
		A_1	391.40	CuO_5 distortion via O_1, O_2, O_3 and O_4 displacement.
R_{10}	527.19	A_1	521.27	Relative displacement of V and O_3, O_4.
		A_2	532.83	Relative displacement of V and O_3, O_4.
R_{11}	649.17	B_1	682.25	In phase displacement of O_3 and O_4 along *a* axis.
		B_2	694.83	VO_4 tetrahedral distortion via O_3 and O_4 displacement.
R_{12}	729.49	A_1	716.78	In phase O_3 displacement along *ac* plane.
		A_2	745.34	Out of phase O_3 displacement along *ac* plane.
R_{13}	789.38	B_1	805.76	Relative displacement of V and O_2, O_4.
		B_2	810.85	VO_4 tetrahedral distortion.
R_{14}	833.51	B_2	843.14	CuO_5 distortion via O_1, O_2 displacement.
R_{15}	863.48	B_1	864.74	CuO_5 distortion via O_1, O_2 displacement.
		A_2	870.03	Out of phase O_1 displacement along *ac* plane.
		A_1	877.18	In phase O_1 displacement along *c* axis.
R_{16}	906.38	A_2	898.98	Out of phase O_2 displacement along *a* axis.
		A_1	905.16	Out of phase O_2 displacement along *a* axis.
		B_2	906.86	In phase relative displacement of O_2 and O_4.
R_{17}	941.24	B_1	916.63	Out of phase relative displacement of O_2 and O_4.

electron-phonon coupling (neglected in α-$Cu_2V_2O_7$ because of its highly insulating character).

In periodic crystal, potential energy can be expanded using Taylor expansion in terms of atomic displacement from their equilibrium position. At absolute zero, the vibrations of atoms in a crystal can be modelled as a linear harmonic oscillator. However, at finite temperature, the vibrations become anharmonic, meaning that the higher-order terms in the periodic potential become important. The anharmonicity of optical phonon modes in the crystal is particularly sensitive to the cubic and quadratic terms in the periodic potential,

$$U(r) = U(r_0) + r\frac{dU}{dr}\bigg|r = r_0 + r^2\frac{dU^2}{dr^2}\bigg|r = r_0 + r^3\frac{dU^3}{dr^3}\bigg|r = r_0 + r^4\frac{dU^4}{dr^4}\bigg|r = r_0 + \cdots \quad (6)$$

The first term in the periodic potential is a constant that does not contribute to the temperature dependence of phonon modes. The second term is linear and goes to zero under

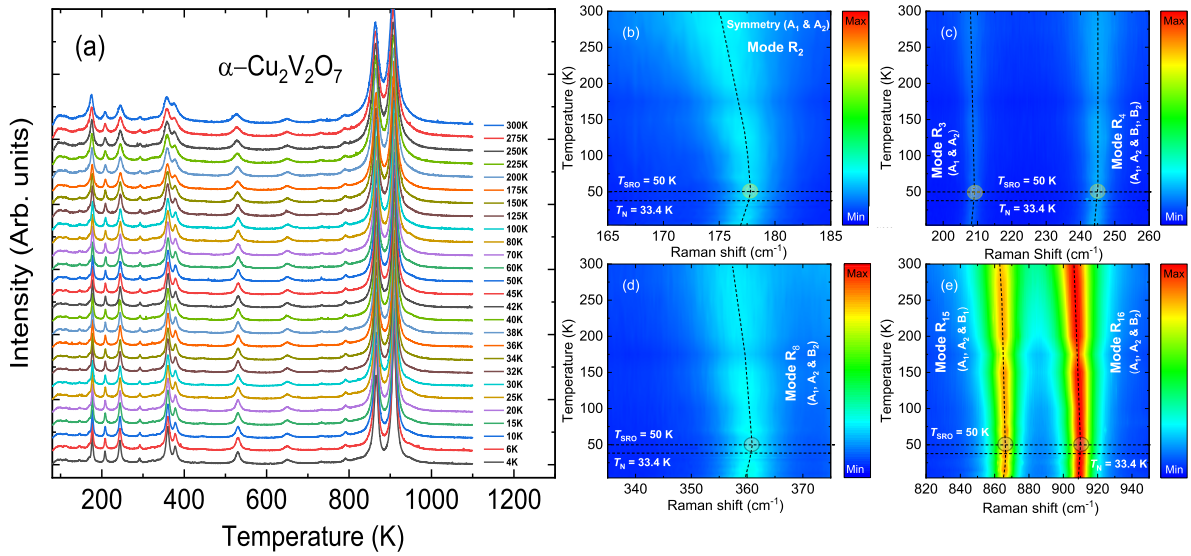

FIG. 8. (a) Temperature-dependent Raman spectra of α-$Cu_2V_2O_7$, the Raman spectra are shifted vertically for clarity. The Raman spectra was acquired at a excitation wavelength $\lambda_{exc} = 633$ nm laser wavelengths. Contour plots depicting evolution of Raman mode frequency as function of temperature for selected Raman modes wavenumber as R_2 (b), R_4 (c), R_8 (d), R_{15}, and R_{16} (e), along with the their respective symmetry elements. The intensity of the Raman modes is represented by color code (right-hand side). Anomalous change in the Raman mode position is highlighted by the filled circle, whereas the dashed horizontal and vertical lines are the guide to the eye.

equilibrium conditions. The third term is quadratic and purely harmonic indicating that it does not contribute to the anharmonicity of phonon modes [71]. The fourth term is cubic and corresponds to the decay of an optical phonon mode into two phonons of equal frequency, i.e., $\omega_1 = \omega_2 = \omega_0/2$. This is known as cubic anharmonicity. The fifth term is quartic and corresponds to the decay of an optical phonon mode into three phonons of equal frequency, i.e., $\omega_1 = \omega_2 = \omega_3 = \omega_0/3$. This is known as quartic anharmonicity. At temperatures below 300 K, the three-phonon processes are sufficient to explain the observed behavior of phonon frequency and damping constant [72,73]. According to three-phonon process the phonon frequency variation with temperature due to cubic anharmonicity is given by [72]

$$\Delta\omega = \omega_0 + A\left[1 + \frac{2}{\exp\left(\frac{\omega\hbar}{2K_BT}\right) - 1}\right]. \tag{7}$$

Similarly, the temperature-dependence of Raman linewidth can be written for three phonon process as [72]

$$\Gamma_{\text{anh}}(T) = \Gamma_0\left[1 + \frac{2}{\exp\left(\frac{\omega\hbar}{2K_BT}\right) - 1}\right]. \tag{8}$$

The deviation of the peak position from the anharmonic curve below the T_N confirms the presence of spin-phonon coupling. The red solid curve, which represents the anharmonic contribution, was obtained by fitting the peak frequency with an anharmonic function above the magnetic ordering temperature and simulating it to lower temperatures. Similarly, the temperature-dependent FWHM was fitted by the Eq. (8). The anharmonic fit of Raman mode and the FWHM fitted Raman spectra is shown in the Fig. 9. Deviation between simulated and experimental data as shown in Fig. 10 gives the frequency modulation influenced by the magnetic ordering and this frequency deviation ($\Delta\omega_{\text{mag}}$) can be described by the equation below [74–76]:

$$\Delta\omega_{\text{mag}} = -\frac{2}{\omega\mu}\frac{\partial^2 J}{\partial u^2}\langle S_i.S_j\rangle = -\lambda_{sp}S^2\phi(T) \tag{9}$$

where $\Delta\ \omega_{\text{mag}}$ indicates deviation in frequency from the anharmonic behavior, $\langle S_i.S_j\rangle$ is spin-spin correlation factor, $\lambda_{sp}(=\frac{2}{\omega\mu}\frac{\partial^2 J}{\partial u^2})$ is the spin-phonon coupling coefficient, J is exchange interactions, ω is frequency of normal mode of vibration and μ is reduced mass, u is vibrational eigen displacement, S^2 denotes average of adjacent spins (in our case $S^2 = \frac{1}{4}$, for Cu^{2+} $3d^9$),

$$\Phi(T) = \left[1 - \left[\frac{T}{T_{SRO}}\right]^{\gamma}\right] \tag{10}$$

where T_{SRO} is short magnetic ordering temperature (50 K), γ is critical exponent. The value of spin-phonon coupling coefficient for various Raman active modes has been calculated and are listed in the Table IV.

The phonon lifetime were calculated via Raman mode linewidth (FWHM) by energy-time uncertainty relation $\tau = \hbar/\Delta E = 1/2\ \pi c\Gamma = 5.3078\,\text{ps}/\Gamma$, where ΔE is uncertainty in phonon energy, τ is phonon lifetime, c is speed of light, Γ is Raman linewidth (in cm^{-1}), $\hbar$ is reduced plank constant. It depends on the anharmonicity, impurities, crystal imperfection, and grain boundaries in the crystal. In a polycrystalline materials, the grain boundaries disrupt the translational symmetry of the crystal lattice, which in turn shortens the lifetime of propagating phonons. This is because phonons can be scattered more easily at grain boundaries, which results in a broader Raman linewidth. Additionally, as the temperature increases, anharmonicity effects become more pronounced, which also contributes to the broadening of the Raman linewidth (Fig. 9). Hence the phonon lifetime τ has been calculated at lowest temperature as 1.04 ± 0.014 ps, $1.27 \pm$

TABLE IV. Spin-lattice constant (λ_{sp}) of the various Raman modes (R) determined by fitting parameters like phonon frequency (ω_0, A) and FWHM (Γ_0) of α-$Cu_2V_2O_7$.

Mode (cm^{-1})	ω_0 (cm^{-1})	A (cm^{-1})	Γ_0 (cm^{-1})	λ_{sp} (cm^{-1})
R_2 (175.05)	179.4 ± 0.6	-1.73 ± 0.68	05.08 ± 0.07	1.92 ± 0.21
R_3 (208.10)	210.7 ± 1.8	-1.72 ± 1.88	04.17 ± 0.07	2.97 ± 0.21
R_8 (357.09)	361.7 ± 0.3	-0.92 ± 0.48	10.84 ± 0.23	2.13 ± 0.23
R_9 (376.08)	383.9 ± 1.1	-4.62 ± 1.10	11.14 ± 0.20	1.45 ± 0.42
R_{10} (527.19)	533.2 ± 0.5	-2.29 ± 0.50	14.71 ± 0.21	1.76 ± 0.16
R_{15} (863.48)	868.3 ± 0.2	-2.05 ± 0.31	11.31 ± 0.51	1.90 ± 0.54
R_{16} (906.38)	912.7 ± 0.4	-2.77 ± 0.44	13.41 ± 0.41	1.55 ± 0.93

0.021 ps, 0.48 ± 0.010 ps, 0.47 ± 0.008 ps, 0.36 ± 0.005 ps, 0.46 ± 0.020 ps, 0.39 ± 0.011 ps for the R_2, R_3, R_8, R_9, R_{10}, R_{15}, and R_{16} Raman modes, respectively. The Figs. 9(a)–9(l) shows a clear deviation of FWHM as a function of temperature below 50 K. This is a clear indication that the lattice is modulated due to magnetic ordering or a signature of strong spin-lattice coupling.

Moreover, an interesting feature we have found in our detailed Raman shift analysis as a function of temperature, which shows a change in the slope in the temperature range of 25–32 K as shown by the blue arrow for the selected R_2, R_8, R_9, and R_{16} modes in Fig. 9. This change in slope is indicative of a lattice structural distortion. Previously, Wang *et al.* [54] found that the thermal expansion coefficient showed weak temperature dependence in the same temperature window, followed by a linear behavior upon cooling. Since Raman is very sensitive with any structural change, therefore, we strongly believe that our detailed temperature-dependent Raman spectroscopy results further confirms that this anomaly is due to local structure distortion around 25 K. However, no signature of structural modification was found in the magnetization or dielectric measurements [54].

IV. DISCUSSION AND CONCLUSIONS

Using our detailed investigations of thermodynamic properties of this compound along with our detailed Raman measurements, we interpret that strong spin-lattice coupling play a key role in α-$Cu_2V_2O_7$ and largely influence the physical properties of this compound. The compound hosts a Cu^{2+} with spin-$\frac{1}{2}$ and is one of the rare experimental realization of coexisting spin sublattices with mixed dimensionalities consisting of 1D zigzag chains and a helical-honeycomb lattice along with frustrating exchange couplings along the diagonal interactions between two conjunctive helical-honeycomb units in the lattice, which appears to be complex 3D network (Fig. 1). However, the analysis of magnetization, specific heat, and temperature-dependent Raman studies suggested that the magnetic properties of α-$Cu_2V_2O_7$ can be explained by J_1 and J_2 exchange couplings as discussed later. Although J_3 is reported to be the leading exchange interaction but is found to be less significant then J_1 and J_2 to explain the experimental magnetic susceptibility by using QMC simulation [29]. Furthermore, the broad maxima in $\chi(T)$ is usually appears for low-dimensional magnetic lattices and is clearly observed for α-$Cu_2V_2O_7$ single crystal suggesting an evidence of the low-dimensional nature [25,29]. Thus, α-$Cu_2V_2O_7$ can be described as a quasi-2D system with anisotropic magnetic interactions in the helical-honeycomb plane ($J_1 \neq J_2$) indicating the mixed dimensionalities of the magnetic spin sublattices.

The CuP_2O_6 is the only one known example, which shows similar mixed dimensionalities and energy scales, where a 1D chains and square lattice are formed due to presence of two spin sublattices [77]. Thermodynamic properties of this CuP_2O_6 compound are well explained by a superposition of the 1D and 2D sublattices. Generally a low-dimensional system is expected to show broad maximum in the susceptibility due to absence of long range spin order in the other dimensions. On the contrary CuP_2O_6 compound does not show broad maximum and only showed a slight kink at the T_N. Below the T_N it shows an increase in the susceptibility due to the presence of DM interactions. It is worth mentioning that the CuP_2O_6 compound is proved to be a low-dimensional antiferromagnet [77]. In both CuP_2O_6 and α-$Cu_2V_2O_7$ polycrystalline compounds, magnetic susceptibility did not show broad maxima due to powder averaging effects and the presence of DM interaction, which substantially suppresses the feature of the broad maxima. The broad maxima due to short-range ordering is usually absent along the direction in which DM interactions are present—for instance in *dc* susceptibility (χ) of α-$Cu_2V_2O_7$ single crystal a broad maxima were present along *b* axis and were absent along *c* axis [25]. Furthermore, the 1D or 2D magnetic lattices without finite DM interactions may renders pronounced broad maxima even on powder samples [78]. Thus, having powder sample and finite DM interactions in α-$Cu_2V_2O_7$ similar to the CuP_2O_6, suggest the presence of mixed dimensionality in this compound as discussed above in the magnetization and heat-capacity sections.

We have calculated NN intrachain interactions from the 1D spin-$\frac{1}{2}$ chain model for α-$Cu_2V_2O_7$, which is found to be $J_1 \sim 62.13$ K. Surprisingly, the calculated interchain exchange coupling parameter J_2 also showed strong coupling and is found to be $J_2 \sim 16.91$ K for the mutually parallel chains under the mean-field approximation. Based on the exchange coupling constants, the nearest-neighbors-coupling constant J_1 is approximately four times larger then J_2. The extracted J_1 interactions from mean field analysis closely matches with obtained J_1 strength from DFT, INS, and QMC simulations [22,24,29], whereas J_2 interaction reasonably matches with J_2 deduced from INS and significantly different than that obtained from DFT calculations as shown in the comparative

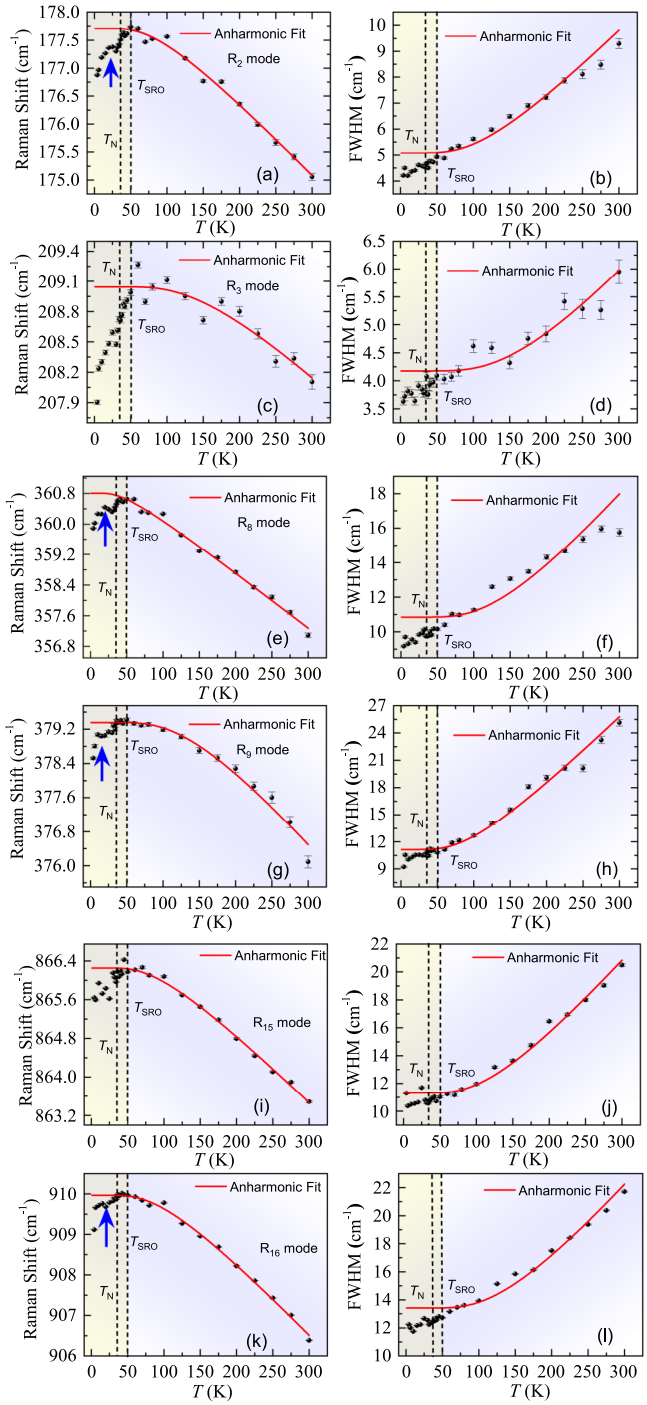

FIG. 9. Raman shift and FWHM of various Raman active mode as a function of temperatures for α-$Cu_2V_2O_7$ [(a)–(l)]. The vertical light yellow filled rectangular box depicts deviation from anharmonic behavior. Moreover, vertical two short-dashed lines are the respective transition temperatures for T_N and T_{SRO}. Whereas, the blue arrows depicts anomaly observed in the Raman Shift.

Table V. This difference in exchange interaction extracted from DFT may be due to consideration of different effective Coulomb interaction (U). Therefore, the spin system has major 1D character as coupled spin chains dominated by J_1 along [011] direction; however, 1D zigzag chains and a 2D helical-honeycomb lattice are coupled to each other, which

TABLE V. Magnetic exchange couplings in α-$Cu_2V_2O_7$. The interatomic distances d_{Cu-Cu} are given in Å. A comparison of the extracted NN magnetic exchange couplings J_1 and J_2 from our χ-fit with reported exchange couplings J_i (in meV), which are theoretically and experimentally calculated by various methods such as DFT [22], INS [24], QMC [29], and χ-fit (this paper) as described in the text. All exchange couplings J_i with–ve sign are antiferromagnetic and +ve sign are ferromagnetic in nature.

d_{cu-cu}	J_i	DFT	INS	QMC	χ-fit
3.139	J_1	−4.67	−4.67	−5.79	−5.35
3.968	J_2	4.07	0.8	2.61	1.45
5.263	J_3	−13.61	–9		

makes the system mixed dimensional in nature as shown in Fig. 1 [22,24,29]. The magnetic structure is frustrated due to presence of coupled J_1, J_2, and J_3 interactions. To further confirm the mix-dimensional character of the magnetic lattice in α-$Cu_2V_2O_7$, we have calculated the ratio of the intrachain and interchain interactions as $J_2/J_{\text{intra}} \simeq 0.272$, which is relatively much larger than that found in 1D chains in many condensed matter systems—for instance, a quasi one-dimensional $BaCu_2Si_2O_7$ compound shows $J_2/J_{\text{intra}} \simeq 0.011$ [42]. This suggests significant 2D character of magnetic lattice along with a less pronounced 1D character present in α-$Cu_2V_2O_7$. As from the previous experimental and theoretical studies along with QMC simulation [25,29], it has been established that J_3 is the leading magnetic interaction, and when this is considered the broad maxima in the susceptibility χ (T) curve can be better fitted, which is observed along only one direction (b axis). However, the experimental susceptibility data other than the broad maxima can be well accounted by only considering J_1 and J_2. This implies that the J_1 and J_2 are the most important exchange couplings to explain the experimental thermodynamic results. On the other hand it is worth to be noted that in the INS spin-wave simulations, anisotropy term is not considered [24], which is crucial as evident from single-crystal anisotropy bulk results [29]. Moreover, in the single crystal of α-$Cu_2V_2O_7$, the appearance of broad maxima in magnetization measurements along the crystallographic b axis is suggesting that it is a low-dimensional magnetic lattice, similarly, our present result on power-law fitting of heat capacity at low temperatures indicated two-dimensional nature and are well corroborated with Raman studies where the spin-phonon coupling can be explained by considering only J_1 and J_2 as discussed in the next paragraph. The local probe nuclear magnetic resonance spectroscopy (NMR) is required as it is an important technique to resolve the dimensionality issue.

The temperature-dependent Raman spectra shows change in the Raman active modes around the magnetic LRO state suggesting that lattice vibrations are strongly coupled with the magnetic ordering. Granado *et al.* [76] proposed that interaction of phonon with the magnetic ordering is manifested by the modulation of exchange integral with the vibrational eigen displacement. In α-$Cu_2V_2O_7$, three exchange interaction terms as J_1, J_2, and J_3 have the main contribution in the mixed dimensional character in the magnetic lattice. J_1 exchange interaction is mediated by two different exchange path ways as Cu-O_3-Cu and Cu-O_1-Cu, whereas J_2 is mediated by

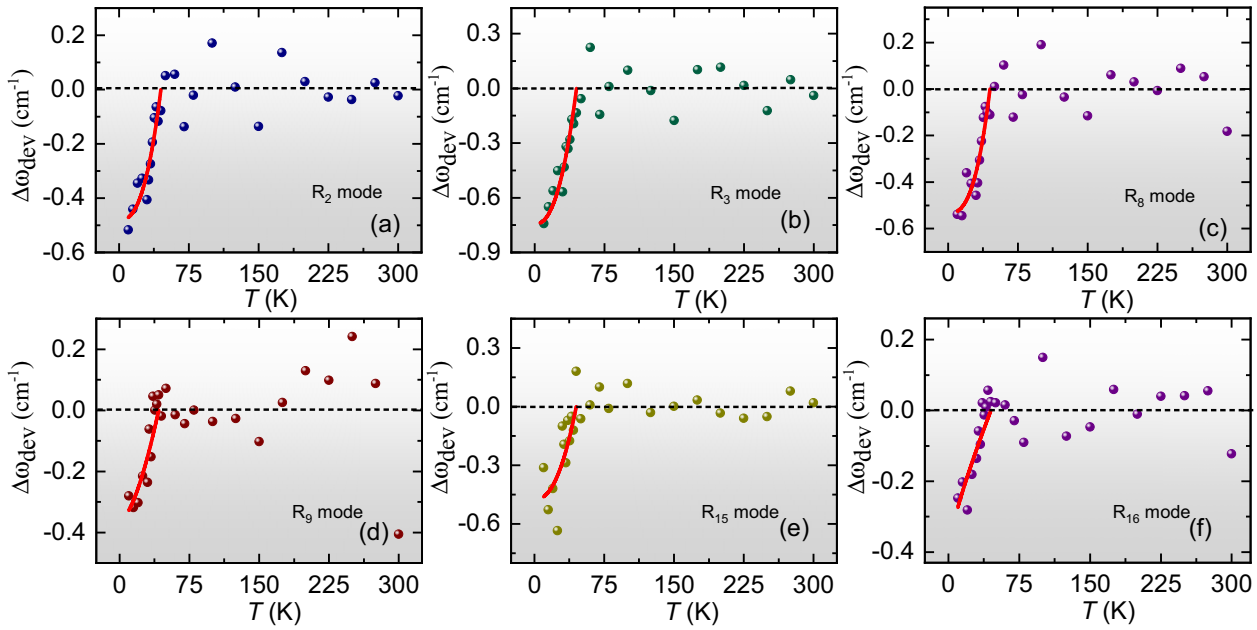

FIG. 10. The deviation of phonon frequency from the anharmonic behavior as function of temperature in α-$Cu_2V_2O_7$ for R_2, R_3, R_8, R_9, R_{15}, and R_{16} modes, respectively. Solid red lines represent fit of spin-phonon coupling below T_{SRO} using Eq. (9).

only single exchange path way as Cu-O_3-O_2-Cu or Cu-O_2-Cu, mostly along the a axis. Finally, the J_3 interaction is mediated by exchange path way as Cu-O_1-V-O_2-Cu [22,79]. These exchange path ways are shown and discussed in Fig. 1. It is worth mentioning that according to x-ray diffraction results [22], the change in the direct bond distance between first- and second-nearest neighbor (related to J_1 and J_2) is observed to be 0.085(2) Å and 0.159(2) Å, respectively when cooled down below 50 K, while the change in the NNN distance (related to J_3) is only 0.01 Å. Therefore, the J_1 and J_2 mostly affect the spin-phonon coupling strength, while J_3 plays minor role. The eigenvector displacements of the phonon modes as R_2, R_3, R_8, R_9, R_{10}, R_{15}, R_{16} are obtained from the DFT calculation, which clearly suggest that the major contribution of the vibrations are found to be from O_1, O_2, O_3 atoms and therefore the eigen displacements of these atoms significantly changes the Cu-O bond lengths as well as Cu-O-Cu bond angles in the crystal lattice, which are affecting mostly J_1 and J_2. Therefore, these bond length and angles further modify the exchange interactions (J_1 and J_2), which couples the phonon modes with the spin degree of freedom as seen below 50 K, resulting in spin-lattice coupling in this compound. Thus, our Raman results support our low-temperature specific heat and magnetization results of α-$Cu_2V_2O_7$ magnetic lattice mainly been driven by J_1 and J_2 and has mixed dimensionality character. Our detailed theoretical as well as experimental Raman analysis under group theory suggest presence of spin-lattice coupling and is found to be (highest value) 2.97 ± 0.21 cm^{-1} for R_3 mode. The present study showed spin-lattice coupling below 50 K, which is well above $T_N \sim 33.4$ K. This showed that strong short-range magnetic interactions remain present in the system up to 50 K. This affects the lattice and hence explain the magnetodielectric behavior reported by Sannigrahi *et al.* [22], where the dielectric constant showed marked changes under the magnetic field below 50 K and spin wave excitations reported by Banerjee *et al.* [24] present up to 50 K. Therefore, α-$Cu_2V_2O_7$ is a peculiar mixed-dimensionality lattice having strong spin-lattice coupling and could be a potential candidate to further study under higher magnetic fields, as it does not show full magnetic saturation up to 56 T [25]. Since our Raman measurements shows interesting spin-lattice properties and to explore further investigation on this polar antiferromagnet, one of the exciting branches could be the high-field Raman studies under magnetic field above H_c.

To summarize, our study provides a comprehensive description of isotropic exchange couplings in the spin-$\frac{1}{2}$ quantum magnet α-$Cu_2V_2O_7$. The structural and magnetic properties of spin-$\frac{1}{2}$ α-$Cu_2V_2O_7$ compound have been investigated by x-ray, magnetic susceptibility, magnetization, heat capacity, XAS, XPS, and Raman spectroscopy. The compound α-$Cu_2V_2O_7$ crystallizes in one of the polar symmetry of orthorhombic crystal structure with space group $Fdd2$ and we interpret this compound as a mixed dimensionalities where the 1D zigzag chains and a 2D helical-honeycomb lattice forms an intricate crystal and magnetic structure. The α-$Cu_2V_2O_7$ compound shows strong spin-lattice coupling below 50 K. Our detailed experimental data show possible signatures of pronounced spin-lattice coupling effects and call for further investigation of α-$Cu_2V_2O_7$ by means of polarized Raman scattering measurements on single crystals in magnetic ordered state.

ACKNOWLEDGMENTS

The work at the UGC-DAE, Consortium for Scientific Research Indore was supported by the Science and Engineering Research Board (SERB), Govt. of India through Grant No. CRG/2022/005666. A.K.Y. acknowledge the financial

support from the Max Planck Society. We acknowledge valuable discussions on triangular-lattice fitting with K. M. Ranjith. The layered perovskite structure figures were prepared using the VESTA software [80].

[1] U. Schollwöck, J. Richter, D. J. J. Farnell, and R. F. Bishop (editors) *Quantum Magnetism* (Springer, New York, 2004).
[2] S. Sachdev, Quantum magnetism and criticality, Nat. Phys. **4**, 173 (2008).
[3] F. Levkovich-Maslyuk, The Bethe ansatz, J. Phys. A: Math. Theor. **49**, 323004 (2016).
[4] J. des Cloizeaux and J. J. Pearson, Spin-wave spectrum of the antiferromagnetic linear chain, Phys. Rev. **128**, 2131 (1962).
[5] S. Nakamura, E. Iyoda, T. Deguchi, and T. Sagawa, Universal scrambling in gapless quantum spin chains, Phys. Rev. B **99**, 224305 (2019).
[6] F. D. M. Haldane, Continuum dynamics of the 1-D Heisenberg antiferromagnet: Identification with the O(3) nonlinear sigma model, Phys. Lett. A **93**, 464 (1983).
[7] T. M. Rice, To condense or not to condense, Science **298**, 760 (2002).
[8] L. Balents, Spin liquids in frustrated magnets, Nature (London) **464**, 199 (2010).
[9] D. A. Sokolov, M. C. Aronson, W. Gannon, and Z. Fisk, Critical phenomena and the quantum critical point of ferromagnetic $Zr_{1-x}Nb_xZn_2$, Phys. Rev. Lett. **96**, 116404 (2006).
[10] Z. He, T. Taniyama, and M. Itoh, Antiferromagnetic-paramagnetic transitions in longitudinal and transverse magnetic fields in a $SrCo_2V_2O_8$ crystal, Phys. Rev. B **73**, 212406 (2006).
[11] M. Isobe, E. Ninomiya, A. N. Vasil'ev, and Y. Ueda, Novel phase transition in spin-$\frac{1}{2}$ linear chain systems: $NaTiSi_2O_6$ and $LiTiSi_2O_6$, J. Phys. Soc. Jpn. **71**, 1423 (2002).
[12] N. D. Mermin and H. Wagner, Absence of ferromagnetism or antiferromagnetism in one- or two-dimensional isotropic Heisenberg models, Phys. Rev. Lett. **17**, 1133 (1966).
[13] K. Binder and A. P. Young, Spin glasses: Experimental facts, theoretical concepts, and open questions, Rev. Mod. Phys. **58**, 801 (1986).
[14] C. Calvo and R. Faggiani, α cupric divanadate, Acta Cryst. B **31**, 603 (1975).
[15] S. Bhowal, J. Sannigrahi, S. Majumdar, and I. Dasgupta, A comparative study of electronic, structural, and magnetic properties of α-, β-, and γ -$Cu_2V_2O_7$, Phys. Rev. B **95**, 075110 (2017).
[16] A. K. Kar, B. Chattopadhyay, R. Singha, A. Barman, M. A. Ahmed, A. Midya, S. Bandyopadhyay, D. Mukherjee, D. Jana and P. Mandal, J. Phys.: Condens. Matter **34**, 075702 (2022).
[17] A. A. Tsirlin, O. Janson, and H. Rosner, β-$Cu_2V_2O_7$: A spin-$\frac{1}{2}$ honeycomb lattice system, Phys. Rev. B **82**, 144416 (2010).
[18] M. Touaiher, K. Rissouli, K. Benkhouja, M. Taibi, J. Aride, A. Boukhari, and B. Heulin, Crystal structures and magnetic properties of $M_2V_2O_7$ (M= Co, Ni and Cu) compounds, Mater. Chem. Phys. **85**, 41 (2004).
[19] Z. He and Y. Ueda, Paramagnetic anisotropy and spin-flop transition in single crystals of the quasi-one-dimensional system β-$Cu_2V_2O_7$, Phys. Rev. B **77**, 052402 (2008).
[20] Z. He, J.-I. Yamaura, Y. Ueda, and W. Cheng, Crystal growth and multiple magnetic transitions of the spin-1 chain system $Ni_2V_2O_7$, Phys. Rev. B **79**, 092404 (2009).
[21] Z. He, J.-I. Yamaura, Y. Ueda, and W. Cheng, Magnetic properties of $Co_2V_2O_7$ single crystals grown by flux method, J. Solid State Chem. **182**, 2526 (2009).
[22] J. Sannigrahi, S. Bhowal, S. Giri, S. Majumdar, and I. Dasgupta, Exchange-striction induced giant ferroelectric polarization in copper-based multiferroic material α-$Cu_2V_2O_7$, Phys. Rev. B **91**, 220407(R) (2015).
[23] J. Sannigrahi, S. Giri, and S. Majumdar, Magnetic and dielectric properties of $Mn_2V_2O_7$, Solid State Commun. **228**, 10 (2016).
[24] A. Banerjee, J. Sannigrahi, S. Bhowal, I. Dasgupta, S. Majumdar, H. C. Walker, A. Bhattacharyya, and D. T. Adroja, Spin wave excitations in the pyrovanadate α-$Cu_2V_2O_7$, Phys. Rev. B **94**, 144426 (2016).
[25] G. Gitgeatpong, M. Suewattana, S. Zhang, A. Miyake, M. Tokunaga, P. Chanlert, N. Kurita, H. Tanaka, T. J. Sato, Y. Zhao, and K. Matan, High-field magnetization and magnetic phase diagram of α-$Cu_2V_2O_7$, Phys. Rev. B **95**, 245119 (2017).
[26] J. U. Lee, S. Lee, J. H. Ryoo, S. Kang, T. Y. Kim, P. Kim, C. H. Park, J. G. Park, and H. Cheong, Ising-type magnetic ordering in atomically thin $FePS_3$, Nano Lett. **16**, 7433 (2016).
[27] Y.-W. Lee, T.-H. Jang, S. E. Dissanayake, S. Lee, and Y. H. Jeong, Magnetism and magnetoelectricity in the polar oxide α-$Cu_2V_2O_7$, Europhys. Lett. **113**, 27007 (2016).
[28] G. Gitgeatpong, Y. Zhao, P. Piyawongwatthana, Y. Qiu, L. W. Harriger, N. P. Butch, T. J. Sato, and K. Matan, Nonreciprocal magnons and symmetry-breaking in the noncentrosymmetric antiferromagnet, Phys. Rev. Lett. **119**, 047201 (2017).
[29] G. Gitgeatpong, Y. Zhao, M. Avdeev, R. O. Piltz, T. J. Sato, and K. Matan, Magnetic structure and Dzyaloshinskii-Moriya interaction in the $S = \frac{1}{2}$ helical-honeycomb antiferromagnet α-$Cu_2V_2O_7$, Phys. Rev. B **92**, 024423 (2015).
[30] A. Pal, T. W. Yen, T. W. Kuo, C. W. Wang, S. M. Huang, M. C. Chou, Y. C. Lai, Y. C. Chuang, P. Yanda, A. Sundaresan, H. S. Kunwar, V. G. Sathe, Ajay Tiwari, D. C. Kakarla, and H. D. Yang, Unconventional multiferroicity induced by structural distortion and magnetostriction effect in the layered spin-1/2 ferrimagnet $Bi_2Cu_5B_4O_{14}$, Phys. Rev. B **107**, 184430 (2023).
[31] A. Pal, C. H. Huang, T. W. Yen, P. H. Lee, Y. H. Chang, C. H. Yeh, T. W. Kuo, A. Tiwari, D. C. Kakarla, S. M. Huang, M. C. Chou, H. S. Kunwar, S. Rana, V. G. Sathe, B. H. Chen, Y. C. Chuang, and H. D. Yang, Spin-induced strongly correlated magnetodielectricity, magnetostriction effect, and spin-phonon coupling in helical magnet $Fe_3(PO_4)O_3$, Phys. Rev. B **106**, 094404 (2022).
[32] Rodríguez-Carvajal, Recent advances in magnetic structure determination by neutron powder diffraction, Phys. B: Condens. Matter **192**, 55 (1993).
[33] G. Kresse and J. Furthmüller, Efficient iterative schemes for *ab initio* total-energy calculations using a plane-wave basis set, Phys. Rev. B **54**, 11169 (1996).
[34] G. Kresse and J. Furthmüller, Efficiency of ab-initio total energy calculations for metals and semiconductors using a plane-wave basis set, Comput. Mater. Sci. **6**, 15 (1996).

[35] G. Kresse and D. Joubert, From ultrasoft pseudopotentials to the projector augmented-wave method, Phys. Rev. B **59**, 1758 (1999).

[36] J. P. Perdew, K. Burke, and M. Ernzerhof, Generalized gradient approximation made simple, Phys. Rev. Lett. **77**, 3865 (1996).

[37] J. P. Perdew, K. Burke, and M. Ernzerhof, Perdew, burke, and ernzerhof reply, generalized gradient approximation made simple, Phys. Rev. Lett. **78**, 1396(E) (1997).

[38] H. J. Monkhorst and J. D. Pack, Special points for Brillouin-zone integrations, Phys. Rev. B **13**, 5188 (1976).

[39] S. V. Krivovichev, S. K. Filaov, P. N. Cherapansky, T. Armbruster, and O. Y. Pankratova, Crystal structure of γ-$Cu_2V_2O_7$ and its comparison to blossite (α-$Cu_2V_2O_7$) and ziesite (β-$Cu_2V_2O_7$), Can. Mineral. **43**, 671 (2005).

[40] J. C. Bonner and M. E. Fisher, Linear magnetic chains with anisotropic coupling, Phys. Rev. **135**, A640 (1964).

[41] H. J. Schulz, Dynamics of coupled quantum spin chains, Phys. Rev. Lett. **77**, 2790 (1996).

[42] I. Tsukada, Y. Sasago, K. Uchinokura, A. Zheludev, S. Maslov, G. Shirane, K. Kakurai, and E. Ressouche, $BaCu_2Si_2O_7$: A quasi-one-dimensional $S = \frac{1}{2}$ antiferromagnetic chain system, Phys. Rev. B **60**, 6601 (1999).

[43] N. Elstner, R. R. P. Singh, and A. P. Young, Finite temperature properties of the spin-1/2 Heisenberg antiferromagnet on the triangular lattice, Phys. Rev. Lett. **71**, 1629 (1993).

[44] H. Rosner, R. R. P. Singh, W. H. Zheng, J. Oitmaa, and W. E. Pickett, High-temperature expansions for the J_1-J_2 Heisenberg models: Applications to *ab initio* calculated models for Li_2VOSiO_4 and Li_2VOGeO_4, Phys. Rev. B **67**, 014416 (2003).

[45] D. C. Johnston, R. K. Kremer, M. Troyer, X. Wang, A. Klümper, S. L. Bud'ko, A. F. Panchula, and P. C. Canfield, Thermodynamics of spin $S = 1/2$ antiferromagnetic uniform and alternating-exchange Heisenberg chains, Phys. Rev. B **61**, 9558 (2000).

[46] A. A. Tsirlin, R. Nath, A. M. Abakumov, R. V. Shpanchenko, C. Geibel, and H. Rosner, Frustrated square lattice with spatial anisotropy: Crystal structure and magnetic properties of $PbZnVO(PO_4)_2$, Phys. Rev. B **81**, 174424 (2010).

[47] See Supplemental Material at http://link.aps.org/supplemental/10.1103/PhysRevB.109.054310 for details of the various eigen displacement for both Raman and Infrared active modes and their respective crystal structure figures at room temperature; Theoretical analytic spin-1/2 models used to calculate theoretical curves for magnetization data, the evidence of mixed-dimensionality of the magnetic-lattice by the theoretical fit of the experimental susceptibility curve using both 1D and 2D spin-1/2 square-lattice, triangular-lattice, and 1D chain-lattice models; comparison of the fitting parameter d (dimensionality of the magnetic lattice) of the low-temperature magnetic contribution (C_{mag}/T^2) part of the heat capacity. The material also contains Refs. [29,40,43–46].

[48] M. E. Lines, Magnetic properties of $CoCl_2$ and and $NiCl_2$, Phys. Rev. **131**, 546 (1963).

[49] C. Kittel, *Introduction to Solid State Physics*, 4th ed. (Wiley, New York, 1966).

[50] E. S. R. Gopal, *Specific Heats at Low Temperatures* (Plenum Press, New York, 1966).

[51] R. J. Goetsch, V. K. Anand, A. Pandey, and D. C. Johnston, Structural, thermal, magnetic, and electronic transport properties of the $LaNi_2(Ge_{1-x}P_x)_2$ system, Phys. Rev. B **85**, 054517 (2012).

[52] A. Yogi, N. Ahmed, R. Nath, A. A. Tsirlin, S. Kundu, A. V. Mahajan, J. Sichelschmidt, B. Roy, and Y. Furukawa, Antiferromagnetism of $Zn_2VO(PO_4)_2$ and the dilution with Ti^{4+}, Phys. Rev. B **91**, 024413 (2015).

[53] A. Yogi, A. K. Bera, A. Maurya, R. Kulkarni, S. M. Yusuf, A. Hoser, A. A. Tsirlin, and A. Thamizhavel, Stripe order on the spin-1 stacked honeycomb lattice in $Ba_2Ni(PO_4)_2$, Phys. Rev. B **95**, 024401 (2017).

[54] L. Wang, J. Werner, A. Ottmann, R. Weis, M. Abdel-Hafiez, J. Sannigrahi, S. Majumdar, C. Koo, and R. Klingeler, Magnetoelastic coupling and ferromagnetic-type in-gap spin excitations in multiferroic α-$Cu_2V_2O_7$, New J. Phys. **20**, 063045 (2018).

[55] K. M. Ranjith, R. Nath, M. Majumder, D. Kasinathan, M. Skoulatos, L. Keller, Y. Skourski, M. Baenitz, and A. A. Tsirlin, Commensurate and incommensurate magnetic order in spin-1 chains stacked on the triangular lattice in $Li_2NiW_2O_8$, Phys. Rev. B **94**, 014415 (2016).

[56] K. M. Ranjith, K. Brinda, U. Arjun, N. G. Hegde, and R. Nath, Double phase transition in the triangular antiferromagnet $Ba_3CoTa_2O_9$, J. Phys.: Condens. Matter **29**, 115804 (2017).

[57] A. Sharma, M. Varshney, K. H. Chae, and S. O. Won, Electronic structure and luminescence assets in white-light emitting $Ca_2V_2O_7$, $Sr_2V_2O_7$ and $Ba_2V_2O_7$ pyro-vanadates: X-ray absorption spectroscopy investigations, RSC Adv. **8**, 26423 (2018).

[58] D. Maganas, M. Roemelt, M. Havecker, A. Trunschke, A. K. Gericke, R. Schlogl, and F. Neese, First principles calculations of the structure and V L-edge x-ray absorption spectra of V_2O_5 using local pair natural orbital coupled cluster theory and spin–orbit coupled configuration interaction approaches, Phys. Chem. Chem. Phys. **15**, 7260 (2013).

[59] G. van der Laan, R. A. D. Pattrick, C. M. B. Henderson, and D. J. Vaughan, Oxidation state variations in copper minerals studied with Cu 2p x-ray absorption spectroscopy, J. Phys. Chem. Solids **53**, 1185 (1992).

[60] M. Grioni, J. B. Goedkoop, R. Schoorl, F. M. F. de Groot, J. C. Fuggle, F. Schafers, E. E. Koch, G. Rossi, J.-M. Esteva, and R. C. Karnatak, Studies of copper valence states with Cu L_3 x-ray-absorption spectroscopy, Phys. Rev. B **39**, 1541 (1989).

[61] J. Zaanen, G. A. Sawatzky, J. Fink, W. Speier, and J. C. Fuggle, $L_{2,3}$ absorption spectra of the lighter $3d$ transition metals, Phys. Rev. B **32**, 4905 (1985).

[62] G. A. Sawatzky and D. Post, X-ray photoelectron and Auger spectroscopy study of some vanadium oxides, Phys. Rev. B **20**, 1546 (1979).

[63] J. Mendialdua, R. Casanova, and Y. Barbaux, XPS studies of V_2O_5, V_6O_{13}, VO_2 and V_2O_3, J. Electron. Spectrosc. Relat. Phenom. **71**, 249 (1995).

[64] G. Silversmit, D. Depla, H. Poelman, G. B. Marin, and R. De Gryse, Determination of the V_{2p} XPS binding energies for different vanadium oxidation states (V^{5+} to V^{0+}), J. Electron. Spectrosc. Relat. Phenom. **135**, 167 (2004).

[65] C. D. Wagner, W. M. Riggs, L. E. Davis, and J. F. Moulder, *Handbook of X-ray Photoelectron Spectroscopy* (Perkin-Elmer Corporation, Minnesota, 1978).

[66] R. P. Vasquez, CuO by XPS, Surf. Sci. Spectra **5**, 262 (1998).

[67] D. Barreca, A. Gasparotto, and E. Tondello, CVD Cu_2O and CuO nanosystems characterized by XPS, Surf. Sci. Spectra **14**, 41 (2007).

[68] D. Tahir and S. Tougaard, Electronic and optical properties of Cu, CuO and Cu_2O studied by electron spectroscopy, J. Phys.: Condens. Matter **24**, 175002 (2012).

[69] H. S. Kunwar, B. K. De, S. Rana, S. Tyagi, G. Sharma, A. K. Rathore, and V. G. Sathe, Investigation of correlation between spin dynamics and lattice degree of freedom in Mott insulator Sr_2IrO_4, AIP Conf. Proc. **2265**, 030564 (2020).

[70] S. Rana, P. Sahlot, V. Dwij, G. sharma, H. S. Kunwar, U. P. Deshpande, D. K. Shukla, and Vasant Sathe, Spin-phonon coupling-mediated magnetodielectricity in B-site disordered $PrFe_{0.5}Mn_{0.5}O_3$, J Mater Sci: Mater Electron **34**, 1802 (2023).

[71] N. W. Ashcroft and N. D. Mermin, *Solid State Physics* (Holt Saunders International Editions, Philadelphia, 1976).

[72] M. Balkanski, R. F. Wallis, and E. Haro, Anharmonic effects in light scattering due to optical phonons in silicon, Phys. Rev. B **28**, 1928 (1983).

[73] P. G. Klemens, Anharmonic decay of optical phonons, Phys. Rev. **148**, 845 (1966).

[74] S. Mahana, B. Rakshit, R. Basu, S. Dhara, B. Joseph, U. Manju, S. D. Mahanti, and D. Topwal, Local inversion symmetry breaking and spin-phonon coupling in the perovskite $GdCrO_3$, Phys. Rev. B **96**, 104106 (2017).

[75] B. Krishna De, V. Dwij, H. S. Kunwar, R. J. Choudhary, and V. G. Sathe, Re-normalization of lattice vibrations below magnetic transition probed by Raman spectroscopy, Phys. B: Condens. Matter **579**, 411806 (2020).

[76] E. Granado, A. García, J. A. Sanjurjo, C. Rettori, I. Torriani, F. Prado, R. Sánchez, A. Caneiro, and S. B. Oseroff, Magnetic ordering effects in the Raman spectra of $La_{1-x}Mn_{1-x}O_3$, Phys. Rev. B **60**, 11879 (1999).

[77] R. Nath, K. M. Ranjith, J. Sichelschmidt, M. Baenitz, Y. Skourski, F. Alet, I. Rousochatzakis, and A. A. Tsirlin, Hindered magnetic order from mixed dimensionalities in CuP_2O_6, Phys. Rev. B **89**, 014407 (2014).

[78] O. Janson, A. A. Tsirlin, J. Sichelschmidt, Y. Skourski, F. Weickert, and H. Rosner, Long-range superexchange in $Cu_2A_2O_7$ (A = P, As, V) as a key element of the microscopic magnetic model, Phys. Rev. B **83**, 094435 (2011).

[79] J. T. Zhang, J. L. Wang, C. Ji, B. X. Guo, W. S. Xia, X. M. Lu, and J. S. Zhu, Magnetism and spin-driven ferroelectricity in the multiferroic material α-$Cu_2V_2O_7$, Phys. Rev. B **96**, 165132 (2017).

[80] K. Momma and F. Izumi, VESTA 3 for three-dimensional visualization of crystal, volumetric and morphology data, J. Appl. Cryst. **44**, 1272 (2011).